Different Magnitudes of Second-Order Jahn-Teller Effect in Isostructural NaMO2F2 (M = Nb5+, Ta5+) Oxyfluorides

Ouail Zakary, Monique Body, Vincent Sarou-Kanian, Brice Arnaud, Gwenaël Corbel, Christophe Legein

Different Magnitudes of Second-Order Jahn-Teller Effect in Isostructural $NaMO_2F_2$ ($M = Nb^{5+}$, Ta^{5+}) Oxyfluorides

Ouail Zakary[a,1,*], Monique Body[a], Vincent Sarou-Kanian[b], Brice Arnaud[a], Gwenaël Corbel[a,*], Christophe Legein[a]

[a] Institut de Molécules et Matériaux du Mans (IMMM) – UMR 6283 CNRS, Le Mans Université, Avenue Olivier Messiaen, 72085 Le Mans Cedex 9, France

[b] CNRS, CEMHTI UPR3079, Université d'Orléans, 45071 Orléans, France

e-mail address of each author:

Ouail.Zakary@oulu.fi; monique.body@univ-lemans.fr; vincent.sarou-kanian@cnrs-orleans.fr; brice.arnaud@univ-lemans.fr; gwenael.corbel@univ-lemans.fr; christophe.legein@univ-lemans.fr

Corresponding Authors:

Ouail.Zakary@oulu.fi (Ouail Zakary); gwenael.corbel@univ-lemans.fr (Gwenaël Corbel)

[1] Present address : NMR Research Unit, Faculty of Science, University of Oulu, P.O. Box 3000, FI-90014 Oulu, Finland

Abstract

The structures of the ordered and isotype oxyfluorides $NaMO_2F_2$ (M = Nb, Ta) were thoroughly investigated by combining powder X-Ray Diffraction (PXRD), ^{19}F and high-field ^{23}Na and ^{93}Nb solid-state NMR, and DFT calculations. The structures, derived from Rietveld refinement of the PXRD data, exclusively consist of *cis*-$[MO_4F_2]^{5-}$ octahedra, in which cations are displaced from their ideal centered positions toward an oxide face. The NMR parameters were calculated for both the experimental (ES) and the atomic positions optimized (APO) structures, the latter exhibiting, as is often the case, the best agreement with the experimental data. Nb^{5+} and Ta^{5+} cations having the same size, niobium and tantalum isotypes have usually very close cell parameters. However, those of $NaNbO_2F_2$ and $NaTaO_2F_2$, particularly *c*, differ in unusual proportions. This difference in *c* parameters is due to stronger second-order Jahn-Teller effect (SOJTE) for the *cis*-$[NbO_4F_2]^{5-}$ than for the *cis*-$[TaO_4F_2]^{5-}$ octahedra, further confirmed by band structure and projected density of states calculations. Furthermore, by optimizing the synthesis conditions of these compounds using thermal analysis, a very low amplitude endothermic event, upon heating, was observed only for $NaNbO_2F_2$. An extensive analysis of the variable temperature (VT) PXRD data revealed that this event is related to a deviation from linearity of the cell parameters evolution and that structural features of these two isotypes evolve differently with temperature.

Keywords

Heteroanionic Materials; oxyfluoroniobiates and oxyfluorotantalates; Second Order Jahn-Teller effect (SOJTE); VT PXRD; Multinuclear solid-state NMR; DFT calculations.

TOC

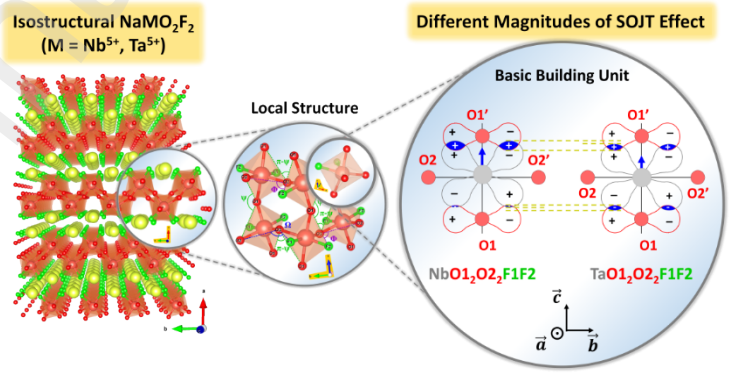

1. Introduction

Inorganic oxyfluorides are heteroanionic materials (HAMs) containing two anionic species with different characteristics, such as charge, ionic radii, electronegativity, and polarizability, which thus offer opportunities to control and tune the electronic and atomic structure and to develop new materials with targeted functionalities [1,2]. In recent years, early transition metal (ETM) d^0 cation (Ti^{4+}, V^{5+}, Nb^{5+}, Ta^{5+}, Mo^{6+} and W^{6+}) oxyfluorides have been investigated for their properties and applications as nonlinear optical (NLO) [3–6], ferroelectric [7,8], photocatalytic [9,10] and battery [11–13] materials.

In HAMs, a metal cation is often bonded to two anionic ligands to form a heteroleptic polyhedron acting as the basic-building unit (BBU) of the structure. The closeness of the ionic radii for oxide and fluoride anions [14] allows them to occupy the same site(s) in a crystal, as for instance in NbO_2F and TaO_2F [15]. However, their different anionic characteristics lead to distinct bonding interactions in the heteroleptic polyhedra: M–O bonds are more covalent and thus shorter compared to the more ionic M–F bonds. These different bond lengths result in M cation displacements toward the oxide ions and produce *cis* rather than *trans* configurations for $[MO_2F_4]^{n-}$ and $[MO_4F_2]^{n-}$ octahedra and *fac* rather than *mer* configurations for $[MO_3F_3]^{n-}$ octahedra. These preferential configurations of ETM d^0 $[MO_xF_{6-x}]^{n-}$ octahedra can lead to structures without anion-site disorder [1], as observed in compounds build on $[MOF_5]^{2-}$ (M = V^{5+}, Nb^{5+}, Ta^{5+} [3,4,16–19]), $[MO_2F_4]^{2-}$ (M = Mo^{6+}, W^{6+} [18,20]), $[MoO_3F_3]^{3-}$ [8,21,22], $[NbO_4F_2]^{5-}$ [6] and $[MO_5F]^{5-}$ (M = Mo^{6+}, W^{6+}) [5,23]. Such distorted octahedra, because of their directing properties, anion ordering and greater probability to crystallize in non-centrosymmetric (NCS) space group are of interest for designing new second harmonic generation (SHG) NLO materials [3,24]. Nevertheless, more often than not, the anion-site order is only partial; between the limits of fully ordered and randomly disordered anions, there are many cases of intermediate anion-site orders with local clustering or extended correlations that may give rise to nonrandom site occupancies in the average crystal structure [1,2]. Among oxyfluoroniobiates and oxyfluorotantalates, correlated disorder manifesting as O/F-ordered strings has been evidenced and modeled in MO_2F [25,15] and MOF_3 [26] resulting, for the latter, from favored *cis*-$[MO_2F_4]^{3-}$ octahedra. Partial orderings are also likely, as observed, for example, in Bi_2NbO_5F [27].

The studied compounds, $NaMO_2F_2$ (M = Nb, Ta), are part of the rich families of sodium oxyfluoroniobiates (V) and oxyfluorotantalates (V) [28], which include for the former, $NaNb_6O_{15}F$ [29], Na_3NbOF_6 [30], Na_2NbOF_5 [31], $NaNb_3O_5F$ [32], $Na_3Nb_{12}O_{31}F$ [33,34] and $Na_2Nb_2O_5F_2$ [35], and for the latter, $Na_2Ta_2O_5F_2$ [35], $Na_2Ta_2O_5F_2$-β [36] and $NaTa_2O_5F$ [37]. Moreover, $Na_2Ta_3O_6F_5$, $Na_4Ta_5O_{10}F_9$, $NaTa_3O_7F_2$, $Na_2Ta_6O_{15}F_2$, $Na_2Ta_8O_{19}F_4$, $NaTa_6O_{15}F$ (isotype with $NaNb_6O_{15}F$) and $NaTa_4O_8F_5$ [38,39] have been reported but their structures have not been determined. Among sodium oxyfluoroniobiates and oxyfluorotantalates whose crystal structures have been reported, only four, $NaMO_2F_2$ (M = Nb [40], Ta), $NaNb_6O_{15}F$ [29] and Na_3NbOF_6 [30], are ordered. $NaNbO_2F_2$ [38,40] and $NaTaO_2F_2$ [38,39], whose atomic positions have not been determined, are isotype and crystallize in the monoclinic system ($P2_1/c$ space group (no. 14)). $NaMO_2F_2$ structures are built up from $[MO_4F_2]^{5-}$ octahedra but $P2_1/c$ is centrosymmetric, which is redhibitory for NLO properties.

In this work, we combine PXRD (for consistency both crystal structures have been refined), ^{19}F, ^{23}Na and ^{93}Nb solid-state NMR and DFT calculations of NMR parameters to characterize the RT structures of $NaMO_2F_2$ (M = Nb, Ta). In the case of ordered structures, as oxide and fluoride anions have very similar X-ray and neutron scattering factors, their structural environments set them apart. Differences in formal charge and size are captured by the popular bond valence sum (BVS) method [41,42]. Due to equal values of ionic radii of Ta^{5+} and Nb^{5+} cations (0.78 Å if sixfold coordinated) [14], niobium and tantalum isotypes have usually very close cell parameters (**Table S1**). $NaNbO_2F_2$ and $NaTaO_2F_2$ are exceptions since their cell parameters, especially *c*, differ in unusual proportions, as a result of a stronger SOJTE for the $[NbO_4F_2]^{5-}$ octahedra in $NaNbO_2F_2$ than for the $[TaO_4F_2]^{5-}$ octahedra in $NaTaO_2F_2$.

Furthermore, in seeking to optimize their synthesis conditions thanks to thermogravimetric and differential thermal analyses (TGA and DTA), a very low amplitude endothermic event upon heating was observed for $NaNbO_2F_2$, but not for its tantalum isotype. The conducted VT PXRD experiments revealed that structural features of the two compounds evolve differently with temperature.

2. Materials and methods

2.1. Sample preparation

$NaNbO_2F_2$ was first synthesized in the form of plate-shaped crystals by Andersson and Galy [40], in the late 1960s, by heating a stoichiometric mixture of NaF and NbO_2F at 600°C. A few years later, single-crystals of $NaTaO_2F_2$ were synthesized by Chaminade et al. [38] who declared it to be an isotype of its niobium counterpart. In the present work, polycrystalline powders of $NaMO_2F_2$ compounds were also obtained from a mixture of NaF and MO_2F (M = Nb, Ta). MO_2F compounds were prepared following the procedure reported in [15], and were subsequently mixed with NaF. As sodium fluoride is moisture sensitive, the steps of weighing, mixing and grinding were carried in a nitrogen-filled glove box. The mixtures were then loaded in platinum tubes, sealed and heated over two days at 550°C and 600°C for $NaNbO_2F_2$ and $NaTaO_2F_2$, respectively. The heating and cooling rates were set to 5°C.min^{-1}.

2.2. Characterization techniques

2.2.1. Solid-state NMR spectroscopy

^{19}F (I = 1/2) magic angle spinning (MAS) NMR spectra were recorded with a Bruker Avance III spectrometer operating at 7 T (Larmor frequency of 282.4 MHz) using a 1.3 mm CP-MAS probe-head. The Hahn echo sequence was used with an interpulse delay of one rotor period and a recycle delay of 20 s. The 90° pulse was set to 1.56 µs (RF field of 160 kHz). For $NaNbO_2F_2$, a ^{93}Nb 64-step small-phase incremental alteration (SPINAL-64) [43] decoupling was employed during the acquisition process at a RF field of ~106 kHz.

^{23}Na (I = 3/2) and ^{93}Nb (I = 9/2) MAS NMR spectra were recorded with a Bruker Avance III spectrometer operating at 20 T (Larmor frequency of 224.9 and 208.1 MHz for ^{23}Na and ^{93}Nb, respectively) using 2.5 and 1.3 mm CP-MAS probe-heads for ^{23}Na and ^{93}Nb, respectively. For ^{23}Na, the spectra were recorded using a heteronuclear ^{23}Na–^{19}F SPINAL-64 decoupling sequence at a RF field of 132 kHz and a recycle delay of 1 s. The pulse duration was set to 0.35 µs (RF field of 36 kHz) corresponding to a small pulse flip angle of 10° to ensure a total excitation of the entire spin system. For the ^{93}Nb static spectrum, the Hahn echo sequence was used with a recycle delay of 1 s, the length of the CT 90° selective pulse was set to 2 µs (RF field of 125 kHz).

The ^{19}F, ^{23}Na and ^{93}Nb spectra were referenced to $CFCl_3$, 1 M NaCl aqueous solution and saturated $K[NbCl_6]/CH_3CN$ solution, respectively. All spectra were fitted using the DMFit software [44].

2.2.2. Thermal analysis

DTA and TGA analyses were carried on ~56 mg powder samples of $NaNbO_2F_2$ and $NaTaO_2F_2$ using a TGA/DTA Q600 SDT TA Instruments apparatus (Pt crucibles, α-Al_2O_3 as a reference) under argon atmosphere (flow rate of 100 $mL.min^{-1}$). The heating process was set from RT to 300°C with heating and cooling rates of 10°$C.min^{-1}$.

2.2.3. Powder X-ray diffraction

Both the RT and the temperature-controlled PXRD patterns were recorded with a PANalytical θ/θ Bragg–Brentano EMPYREAN diffractometer ($CuK\alpha_{1+2}$ radiations) equipped with a PIXcel^{1D} detector. The RT PXRD patterns were measured in a 2θ range of 5° to 135° with a 0.0131° step size. The total acquisition time was approximately 7h30. The raw powders were dusted through a 63 µm sieve (Saulas) on a glass holder to avoid the strong preferential grain orientation. The temperature-controlled PXRD patterns were recorded under air in a temperature ranging from RT to 300°C using a HTK 900 Anton Paar furnace attachment and a glass ceramic Macor sample holder. The PXRD patterns were collected at intervals of 20°C and 10°C over the temperature ranges [25–220°C] and [220–300°C], respectively (heating rate of 5°C/min). The temperature was stabilized for 20 minutes before each pattern was recorded. Each PXRD pattern was collected at a given temperature over a 2θ range from 10° to 100° with a 0.0131° step size and a total acquisition time of 3 h.

2.3. First principle calculations

Our first-principles calculations, based on density functional theory (DFT) [45], were all performed using the VASP code (version 6.2.1) [46,47], with a wave function expanded on a plane-wave basis set with a 550 eV kinetic energy cut-off and (4 × 6 × 4) shifted Monkhorst-Pack k-point mesh. These calculations used the Perdew–Burke–Ernzerhof functional including the generalized gradient approximation (GGA-PBE) [48] to obtain the ground state electronic structure. The interactions between core and valence electrons were described using the projector augmented wave (PAW) method [49], with cores configurations of [He] for O, F and Na, [Ar], $3d^{10}$ for Nb and [Xe], 4f14 for Ta and the PAW potentials O_s_GW, F_GW, Na_sv_GW, Nb_sv_GW and Ta_sv_GW, for O, F, Na, Nb and Ta respectively, including six

electrons for O ($2s^2\ 2p^4$), seven electrons for F ($2s^2\ 2p^5$), nine electrons for Na ($2s^2\ 2p^6\ 3s^1$) and thirteen for Nb ($4s^2\ 4p^6\ 4d^5$) and Ta ($5s^2\ 5p^6\ 5d^5$). The atomic positions were relaxed until all forces converged to less than 0.1 meV/Å. The total energy was converged up to change below 10^{-8} eV.

The PAW [49,50] and the gauge including projector augmented wave (GIPAW) [51,52] approaches were used to calculate the quadrupolar coupling NMR parameters and the magnetic shielding values, respectively. The PAW potentials, plane-wave energy cut-off and the shifted Monkhorst-Pack k-point mesh were set the same as the DFT relaxation.

2.4. Tensor convention and magnetic shielding to chemical shift conversion

The calculated magnetic shielding tensor and the experimental chemical shift parameters are defined by the Haeberlen convention [53]. The isotropic magnetic shielding (σ_{iso}), the anisotropy of the magnetic shielding (σ_{CSA}) and the asymmetry parameter (η_{CSA}), are respectively defined as $\sigma_{iso} = (\sigma_{xx} + \sigma_{yy} + \sigma_{zz})/3$, $\sigma_{CSA} = \sigma_{zz} - \sigma_{iso}$ and $\eta_{CSA} = (\sigma_{yy} - \sigma_{xx})/\sigma_{CSA}$, with the magnetic shielding tensor components σ_{ii} defined in the sequence $|\sigma_{zz} - \sigma_{iso}| \geq |\sigma_{xx} - \sigma_{iso}| \geq |\sigma_{yy} - \sigma_{iso}|$. Similarly, the chemical shift tensor is defined by three parameters, the isotropic chemical shift (δ_{iso}), the anisotropy of the chemical shift (δ_{CSA}) and the asymmetry parameter (η_{CSA}), which are given by $\delta_{iso} = (\delta_{xx} + \delta_{yy} + \delta_{zz})/3$, $\delta_{CSA} = \delta_{zz} - \delta_{iso}$ and $\eta_{CSA} = (\delta_{yy} - \delta_{xx})/\delta_{CSA}$, with the chemical shift tensor components defined in the sequence $|\delta_{zz} - \delta_{iso}| \geq |\delta_{xx} - \delta_{iso}| \geq |\delta_{yy} - \delta_{iso}|$. σ_{iso} is related to δ_{iso} by the relation: $\delta_{iso} \simeq \sigma_{iso,ref} - \sigma_{iso}$, with $\sigma_{iso,ref}$ being the absolute isotropic magnetic shielding reference.

In the present work, ^{23}Na and ^{93}Nb δ_{iso} values were obtained using previously established linear regressions $\delta_{iso} = -0.811(13)\ \sigma_{iso} + 449(7)$ [54] and $\delta_{iso} = -\sigma_{iso} - 586.9$ [15], respectively. For ^{19}F δ_{iso} values, two new linear regressions, established from NaF [55] and $NaNbO_2F_2$ or $NaTaO_2F_2$, were used.

3. Results and discussion

3.1 RT PXRD data refinements

The experimental structures (ES) were obtained by refining the recorded RT PXRD diagrams using the structural Rietveld refinement method [56] implemented in the Fullprof software [57]. The crystal structure of $NaNbO_2F_2$ [40] was used as initial model for the refinements. Isotropic displacement parameters (IDPs, U_{iso}) were considered for all atoms. The background intensity was estimated from linear interpolation between points manually selected in regions free from Bragg reflections. The crystallographic data are gathered in **Table 1**. The atomic coordinates and U_{iso} values are gathered in **Table 2**. The observed, calculated and intensity difference patterns and reliability factors are given as supplementary material (**SM**) (**Fig. S1** and **S2**). Crystal structures have been deposited via the joint CCDC/FIZ Karlsruhe deposition service. CSD [58] 2298195 and 2298196 (deposition number) contain the supplementary crystallographic data for $NaNbO_2F_2$ and $NaTaO_2F_2$, respectively. These data can be found free of charge from FIZ Karlsruhe via https://www.ccdc.cam.ac.uk/structures.

The cell parameters differ slightly compared with those determined previously : a = 8.013 Å (a different value is also reported (8.063 Å) in the abstract of the paper), b = 5.405 Å, c = 7.626 Å and β = 101.70 (°), *i.e.*, V = 323.42 Å^3 (325.44 Å^3) for $NaNbO_2F_2$ [40] and a = 8.091 Å, b = 5.434 Å, c = 7.498 Å and β = 102.15 (°), *i.e.*, V = 322.28 Å^3 for $NaTaO_2F_2$ [39]. As mentioned in the introduction, the cell parameters of $NaNbO_2F_2$ and $NaTaO_2F_2$, whether determined more than 50 years ago or for this study, differ in unusual proportions compared with others niobium and tantalum isotypes (**Table S1**): –1.2 % and +1.7 % from Nb to Ta, for a and c, respectively. These differences almost perfectly compensate since the volumes of the two cells differ by less than 0.1 %.

The BVS values gathered in **Table 3** were calculated using the following values of R_0 parameters: 1.756 [59], 1.677, 1.911, 1.92 [41], 1.87 and 1.88 Å [42] for Na^+/O^{2-}, Na^+/F^-, Nb^{5+}/O^{2-}, Ta^{5+}/O^{2-}, Nb^{5+}/F^- and Ta^{5+}/F^- ion pairs, respectively, and b = 0.37 Å. They support the refined crystal structures and then the ordering proposed previously for $NaNbO_2F_2$ [40].

Table 1. Crystal data for $NaNbO_2F_2$ and $NaTaO_2F_2$.

	$NaNbO_2F_2$	$NaTaO_2F_2$
Crystal system	monoclinic	
SG	$P2_1/c$	
a (Å)	8.0026(3)	8.09997(3)
b (Å)	5.4072(3)	5.4391(1)
c (Å)	7.6243(3)	7.4982(3)
β (°)	101.916(2)	102.128(2)
V (Å^3)	322.81(2)	322.96(1)
Z	2	
Formula weight (g.mol^{-1})	371.7656	547.8488
Density (calculated, g.cm^{-3})	3.825	5.634
T (K)	298	
Wavelength ($K\alpha_1/K\alpha_2$) (Å)	1.54056/1.54433	
2θ range (°)	5–135	
$R_p/R_{wp}/R_{exp}$ (%)	10.8/11.4/2.3	9.2/9.2/2.0
R_B/R_F (%)	6.2/5.2	5.0/5.3

Table 2. Atom, atomic coordinates (x, y, z) and isotropic displacement parameter (U_{iso}, Å^2) of $NaNbO_2F_2$ and $NaTaO_2F_2$. All atoms fully occupy 4e Wyckoff positions (symmetry 1).

	$NaNbO_2F_2$				$NaTaO_2F_2$			
Atom	***x***	***y***	***z***	U_{iso}	***x***	***y***	***z***	U_{iso}
Na1	0.3666(9)	0.780(3)	0.116(1)	0.014(3)	0.377(1)	0.793(3)	0.109(2)	0.014(5)
Nb1/Ta1	0.1549(3)	0.2644(9)	0.3180(4)	0.017(1)	0.1581(2)	0.2598(6)	0.2982(2)	0.0060(3)
O1	0.183(2)	0.156(2)	0.071(2)	0.018(4)	0.199(2)	0.154(3)	0.053(3)	0.007(5)
O2	0.043(2)	0.544(3)	0.212(2)	0.018(4)	0.037(3)	0.559(4)	0.216(3)	0.007(5)
F1	0.377(2)	0.444(2)	0.314(2)	0.023(4)	0.376(2)	0.472(3)	0.304(3)	0.014(4)
F2	0.310(2)	0.977(2)	0.378(2)	0.023(4)	0.330(2)	0.982(3)	0.377(3)	0.014(4)

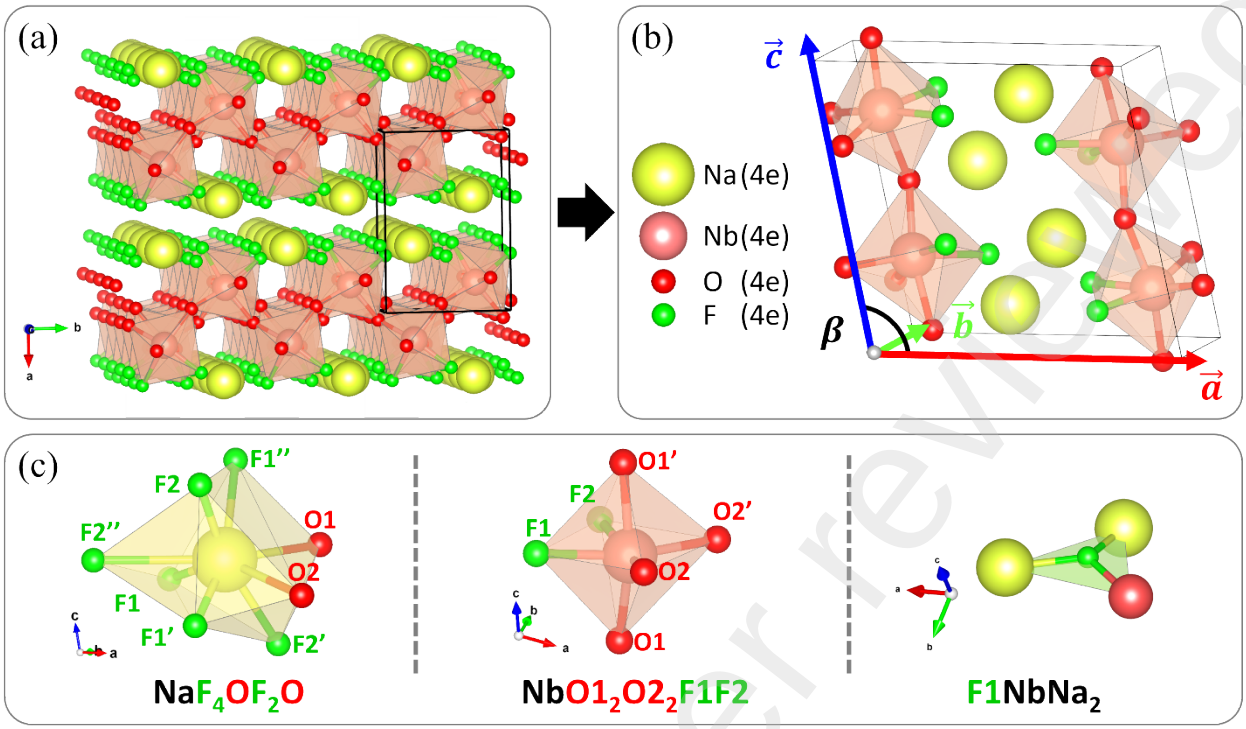

Fig. 1. Perspective views of the (a) $(NbO_2F_2^-)_n$ layers in the structure of $NaNbO_2F_2$, (b) of the unit cell and (c) of the coordination polyhedra of Na and Nb sites and one of the F sites, in which, atoms labeled X, X' and X'' (X = O1, O2, F1 and F2) are equivalent by symmetry operations. The drawings were created using VESTA [60].

Perspective views of the structure of $NaNbO_2F_2$ illustrating the $(NbO_2F_2)_\infty$ layers, the unit cell and the local environments of Na^+, Nb^{5+} and F^- ions are represented in **Fig. 1**. In $NaMO_2F_2$, the $[MO_4F_2]^{5-}$ octahedra adopt, as expected, a *cis* configuration and only share their four oxygen vertices with each other to build infinite $(NbO_2F_2)_\infty$ layers with outward-facing fluorine vertices. This is consistent with the strong affinity between the electropositive sodium and the most electronegative fluorine. Concurrently, the Nb^{5+} cations displace toward the oxide ions located *trans* to the fluoride ones, increasing the overall bonding strength and enhancing the inherent distortions of the heteroleptic $[MO_4F_2]^{5-}$ octahedra (**Fig. 1(c)**, M–X bond lengths and X–M–X angles are reported in **Tables 4** and **S4,** respectively). The wavy $(NbO_2F_2)_\infty$ layers are stacked along the crystallographic *a* axis and separated from each other by Na^+ ions located in an irregular environment consisting of six F^- ions and two O^{2-} ions, in the sequence 4/1/2/1 (**Table S3** and **Fig. 1(c)**). It was described

by Andersson *et al.* as a distorted octahedra considering only the F^- ions or as sevenfold coordinated considering in addition the nearest O^{2-} ion [40]. Na^+ conduction properties were investigated in both the stoichiometric and sodium-deficient $NaNbO_2F_2$ phases but the ionic conductivity of both samples «could not be measured because they were too porous» [61].

The larger *c* value observed for $NaNbO_2F_2$ results from longer Nb–O1 bond lengths (**Table 4** and **Fig. 1(c)**) and larger Nb–O1–Nb (147.8°) and O1-Nb-O1 (166.9°) angles compared with their counterparts in $NaTaO_2F_2$ (143.9° and 161.1°, **Fig. 1(b)**). The lower *a* value observed for $NaNbO_2F_2$ is related to the lower thickness of the $(NbO_2F_2^-)_n$ layers (~5.394 Å) compared to $(TaO_2F_2^-)_n$ layers (~5.599 Å) in $NaTaO_2F_2$ (**Fig. 1(a)**). Further details are discussed in section 3.6.

Table 3. Bond valence sum values from ES and APO models of $NaMO_2F_2$ (M = Nb & Ta)

M	Model	V_i^{Na}	V_i^{M}	V_i^{O1}	V_i^{O2}	V_i^{F1}	V_i^{F2}
Nb	ES	1.003	5.069	1.783	2.070	1.107	1.112
	APO	1.021	5.013	1.922	1.972	1.076	1.064
Ta	ES	1.103	4.926	1.915	2.027	1.067	1.021
	APO	1.020	5.135	1.980	2.011	1.094	1.070

Table 4. Individual and average M–X bond lengths (X = O1, O1', O2, O2', F1 and F2, Å) in the $[MO_4F_2]^{5-}$ octahedra in the ES and APO models of $NaMO_2F_2$ (M = Nb & Ta) and in the structure of $NaNbO_2F_2$ determined earlier from single crystal (SC) [40].

$NaMO_2F_2$	**M = Nb**			**M = Ta**	
Model	**ES**	**APO**	**SC**	**ES**	**APO**
M–F1	2.03(2)	2.04	2.04	2.11(2)	2.05
M–F2	1.99(1)	2.02	2	2.06(2)	2.02
M–O1	1.94(2)	1.83	1.83	1.93(2)	1.94
M–O1'	2.03(2)	2.14	2.12	2.02(2)	1.97
M–O2	1.86(2)	1.94	1.93	1.93(2)	1.93
M–O2'	1.96(2)	1.90	1.88	1.90(2)	1.92
<M-X>	**1.97**	**1.98**	**1.97**	**1.99**	**1.97**

3.2 Multinuclear solid-state NMR

High-resolution solid-state NMR data are essential to support a structure determination through powder diffraction techniques. Indeed, for each observed nucleus, NMR spectra provide information about the number of non-equivalent crystallographic sites and their relative multiplicity. In addition, NMR data can be used in conjunction with DFT calculations to assess the accuracy of structural models.

The experimental ^{19}F, ^{23}Na and ^{93}Nb NMR spectra and their fits are gathered in **Fig. 2** and the experimental NMR parameters relevant for the discussion, including δ_{iso}, δ_{CSA}, η_{CSA}, the quadrupolar coupling constant (C_Q) and the asymmetry parameter (η_Q) are reported in **Table 5**. More details on the ^{23}Na spectra and on the ^{19}F and on the ^{23}Na experimental NMR parameters are given as **SM** (**Fig. S3-S4** and **Tables S6-S8)**.

3.2.1 ^{19}F NMR

Both recorded ^{19}F MAS NMR spectra (**Fig. 2 (a)** and **(b)**) present two main resonances with similar intensities, as expected for two F crystallographic sites of same multiplicity (4e), as well as low intensity resonances assigned to NaF (δ_{iso} = –224.2 ppm [62]) and unidentified impurities. Two or three contributions were used to reconstruct each main resonance perfectly (**Tables S6** and **S7**). The ^{19}F δ_{iso} values (**Table 5**) are in between those of NaF in which F^- ions are sixfold coordinated to Na^+ ions (2.32 Å [55]) and those of the terminal F^- ions in NbF_5 (193-268 ppm [63]), $KNbF_6$ (100.0 ppm [64]), $CsNbF_6$ (110.1 ppm [65]), TaF_5 (106-174 ppm [63]), and $KTaF_6$ (37.1 ppm [64]). Accordingly, the δ_{iso} values of $NaNbO_2F_2$ are higher than those of $NaTaO_2F_2$. The significantly lower values for $NaNbO_2F_2$ and $NaTaO_2F_2$ compared with the NbF_5 and TaF_5 ones can be explained by the presence of (two close) Na^+ ions (**Table 6**) and longer Nb–F and Ta–F bond lengths in $NaNbO_2F_2$ and $NaTaO_2F_2$ (the shortest the bond length, the largest the δ_{iso} value [63,66]). The same last argument and the larger δ_{iso} values of KF (–133.2 ppm [62]) and CsF (–11.2 ppm [62]) compared to NaF, explains the significantly lower values compared with $KNbF_6$ (2 F sites, doubtful bond lengths: Nb–F1,2 = 2.124, 2.130 Å [67]), $CsNbF_6$ (Nb-F = 1,876 Å [68]) and $KTaF_6$ (3 F sites, Ta–F(1,2,3) = 1.905, 1.930, 1.905 Å [69]). The δ_{iso} gaps between the two main lines are similar: 27.8 and 21.5 ppm for $NaNbO_2F_2$ and $NaTaO_2F_2$, respectively. The main difference between the environment of F1 and F2 in $NaNbO_2F_2$ and $NaTaO_2F_2$ relies on the F–Nb and F–

Ta bond lengths which are shorter for F2 (**Table 4**). Then, for each compound, the ^{19}F resonance with a lower (higher) δ_{iso} value is tentatively assigned to the F1 (F2) atoms.

3.2.2 ^{23}Na and ^{93}Nb NMR

^{23}Na ($I = 3/2$) and ^{93}Nb ($I = 9/2$) are subjected to quadrupolar interaction. In this case, the use of high magnetic fields considerably improves the resolution in MAS spectra, since the chemical shift dispersion increases with the magnetic field while second-order quadrupolar broadenings decrease [70]. The use of high magnetic fields are most beneficial for niobium compounds with large ^{93}Nb quadrupolar coupling constants (exceeding 20 MHz) [71]. The shapes of the central transition (CT) of the high magnetic field NMR spectra of ^{23}Na and ^{93}Nb (**Fig. 2 (c**, **d, e)**) are indicative of large η_Q values consistent with the low symmetry (1) of these distorted sites.

While most of the ^{93}Nb C_Q values in homoleptic octahedra do not exceed 30 MHz for oxides [71] and are around 10 MHz for fluorides [64,65], the off-centering of Nb^{5+} in the heteroleptic *cis*-$[NbO_4F_2]^{5-}$ and $[NbOF_5]^{2-}$ octahedra results on larger ^{93}Nb C_Q values (42.0 MHz in $NaNbO_2F_2$ (**Table 5**), 36.0 and 33.2 MHz in $Cdpy_4NbOF_5$ (py = C_5H_5N) and $[pyH]_2[Cdpy_4(NbOF_5)_2]$ [72]). The ^{93}Nb δ_{iso} values for $[NbO_{6-x}F_x]^{(7-x)-}$ octahedra decrease as x increases: between –900 and –1100 ppm for most of the $[NbO_6]^{7-}$ octahedra [71], close to –1300 ppm for $[NbOF_5]^{2-}$ octahedra (–1310 and –1320 ppm [72]) and around –1600 ppm for $[NbF_6]^-$ octahedra [64,65]. The ^{93}Nb δ_{iso} value for $[NbO_4F_2]^{5-}$ octahedron in $NaNbO_2F_2$ (**Table 5**) respects this trend.

The satellite transitions (STs) in the ^{23}Na spectrum of $NaTaO_2F_2$ are significantly less intense than those in the well reconstructed ^{23}Na spectrum of $NaNbO_2F_2$ (**Fig. S3** and **S4**). The shape of the STs in the ^{23}Na spectrum of $NaTaO_2F_2$ is perfectly Lorentzian, so this undoubtedly reflects a dynamic effect. Two 'Int2quad' [44] lines with the same chemical shifts and quadrupolar parameters, one for the central transition (CT) and the second for the STs, were used to reconstruct the spectrum, allowing the intensity and width of the transitions to be adjusted separately (**Table S8**). The NMR parameters of ^{23}Na in the two isotypes are close, as expected for Na^+ similar environments (**Table 5**). The C_Q values are in the same order of magnitude than those observed for eightfold-coordinated sodium

fluorides in α-$NaCaAlF_6$ (Na1, C_Q = 1.36 MHz) [73], $Na_5Al_3F_{14}$ (Na1 and Na2, C_Q = 1.48 and 3.18 MHz) and Na_3AlF_6 (Na2, C_Q = 1.43 MHz) [74].

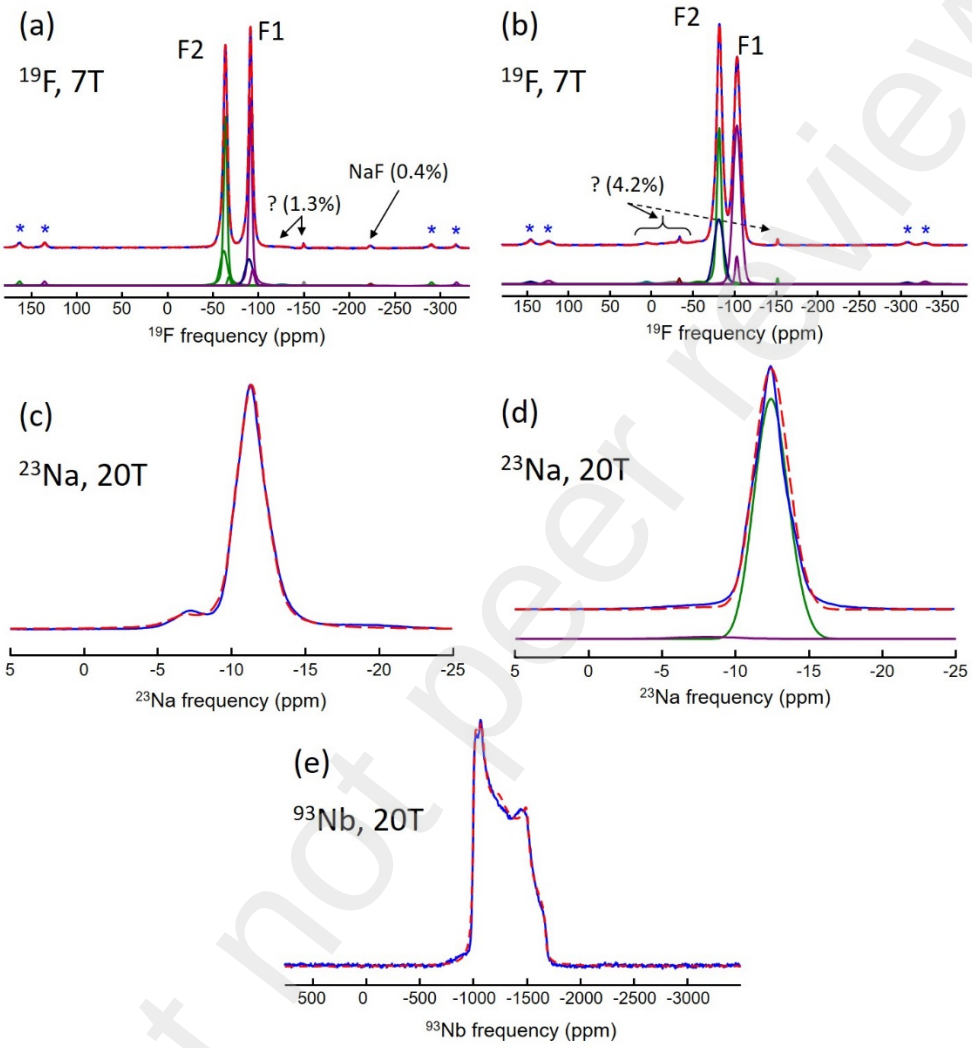

Fig. 2. Experimental (blue) and fitted (dashed red) MAS NMR spectra of (a) ^{19}F (64 kHz), (c) CT of ^{23}Na (30 kHz) and (e) static NMR spectra of ^{93}Nb for $NaNbO_2F_2$ and MAS NMR spectra of (b) ^{19}F (64 kHz) and (d) CT of ^{23}Na (30 kHz) for $NaTaO_2F_2$. On the ^{19}F spectra and on the ^{23}Na CT of $NaTaO_2F_2$, the individual resonances used for the fits (**Tables S6-S8**) are shown below. On the ^{19}F spectra, the stars indicate spinning sidebands, the main resonances are assigned and additional resonances, one assigned to NaF and the other to unidentified impurities, are outlined and their relative intensities are indicated.

Table 5. Compound, nuclei, experimental δ_{iso}, δ_{CSA} (ppm), and η_{CSA} values for all observed nuclei, C_Q (MHz) and η_Q values for ^{23}Na and ^{93}Nb, relative intensities (I, %) and corresponding assignments for ^{19}F.

Compound	Nucleus	δ_{iso}	δ_{CSA}	η_{CSA}	C_Q	η_Q	I	Assignment
$NaNbO_2F_2$	**^{19}F**	-90.8	-125	0			49.0	F1
		-63.0	-130	0			49.4	F2
	^{23}Na	-9.8	8.9	0.30	1.60	0.71		
	^{93}Nb	-1206.1	-285.2	0.08	42.0	0.60		
$NaTaO_2F_2$	**^{19}F**	-102.8	-117.4	0			46.2	F1
		-81.3	-127.2	0			49.6	F2
	^{23}Na	-11.2	8.5	0.30	1.74	0.67		

Table 6. F–M bond lengths (X = F1 and F2, Å) from the ES and APO models of $NaMO_2F_2$ (M = Nb, Ta).

$NaMO_2F_2$	**M = Nb**		**M = Ta**	
Model	**ES**	**APO**	**ES**	**APO**
F1–M	2.03(2)	2.04	2.11(2)	2.05
F1–Na1	2.22(2)	2.26	2.20(2)	2.27
F1–Na1'	2.35(2)	2.29	2.28(3)	2.31
F2–M	1.99(1)	2.02	2.06(2)	2.02
F2–Na1	2.25(2)	2.26	2.27(2)	2.25
F2–Na1'	2.39(2)	2.35	2.35(2)	2.37

3.3 DFT relaxation

In order to assess the quality of the crystal structures and to confirm the ^{19}F resonance assignments, NMR parameters were modeled, for each compound, from both the experimental (ES) and atomic position optimized (APO) crystal structures.

Table 7. Distortion index (*DI*), quadratic elongation ($\langle\lambda\rangle$), bond angle variance (σ_θ, deg.^{2}) and d_{X-M-X} - $\langle d\rangle$ (Å) with d_{X-M-X} the *s*um of two opposite M–X (M = Nb, Ta; X = O, F) bond lengths and $\langle d\rangle$ the mean d_{X-M-X} distance for the $[MO1_2O2_2F1F2]^{5-}$ octahedra in $NaNbO_2F_2$ and $NaTaO_2F_2$ calculated from ES and APO models.

Compound	Model	*DI*	$\langle\lambda\rangle$	σ_θ	$d_{O1-M-O1}$-$\langle d\rangle$	$d_{F1-M-O2}$-$\langle d\rangle$	$d_{F2-M-O2}$-$\langle d\rangle$
$NaNbO_2F_2$	ES	0.025	1.016	50.8	0.038	0.053	-0.090
	APO	0.044	1.015	42.8	0.013	-0.012	0.000
$NaTaO_2F_2$	ES	0.034	1.015	48.5	-0.036	0.0027	0.010
	APO	0.023	1.008	26.0	-0.036	0.0026	0.009

Focussing now on the relaxation effects with respect to the ES, as is often the case for powder-refined crystal structures, significant atomic displacements (up to 0.11 Å for O in $NaNbO_2F_2$) are observed for $NaNbO_2F_2$ and $NaTaO_2F_2$ (**Table S2**). Nevertheless, the average bond lengths evolve little in the *cis*-$[MO_4F_2]^{5-}$ octahedra (**Table 4**) and in the Na^+ ions polyhedra (**Table S3**). The angular distortions in the *cis*-$[MO_4F_2]^{5-}$ octahedra, $\alpha = \frac{1}{12}\sum_{i=1}^{n}|\alpha_i - 90°|$ and $\beta = \frac{1}{3}\sum_{i=1}^{n}|\beta_i - 180°|$ with α_i the twelve angles between two adjacent M–X bonds and β_i the three angles between two opposite M–X bonds (**Table S4**) are slightly reduced for $NaNbO_2F_2$. They are further reduced for $NaTaO_2F_2$ and are thus stronger in the APO structure of $NaNbO_2F_2$ than in that of $NaTaO_2F_2$. These observations are corroborated by the evolution of the values of the distortion index [75], quadratic elongation (λ) and bond angle variance (σ_θ) [76] of the *cis*-$[MO_4F_2]^{5-}$ octahedra (**Table 7**). Unsurprisingly, for $NaNbO_2F_2$, the structural characteristics of the APO model are closer to the structure determined on single crystal (**Table 4**), confirming its accuracy [40].

As expected, for both the ES and APO models, the M–F bonds are longer than the M–O2 bonds (**Table 4**) and the O2–M–O2 angles are larger (ranging from 96 to 98°) than the F1–M–F2 angles (ranging from 82 to 84°, **Table S4**). In the APO structures, M–F bond lengths, on the one hand, and M–O2 bond lengths, on the other hand, are close. However, there is a markedly different structural feature in the two compounds; while the M–O1 bond lengths differ slightly from each other and to the same extent in each of the two ES (~0.09 Å), they

differ significantly (~0.31 Å) in $NaNbO_2F_2$ APO and almost not at all in $NaTaO_2F_2$ APO (~0.03 Å). The *c* parameter is equal to the distance between two O1 atoms of two *cis*-$[MO_4F_2]^{5-}$ octahedra sharing a O1 atom (**Fig. 1**), and therefore depends on the lengths of the M–O1 bonds and on the values of the O1–M–O1 and M–O1–M angles. Consequently, the longer Nb–O1 (shorter Ta–O1) bonds are consistent with a higher (lower) *c* value for $NaNbO_2F_2$ ($NaTaO_2F_2$). To verify that the divergence in cell parameters is not due to inaccuracies in structural refinements, they have been fully optimized. This results in slight increases in the cell parameters values (ranging from 0.3% to 1.1%). Nevertheless, the ratios of the parameters *a* on the one hand (0.986) and *c* on the other hand (1.013) remain far from 1 (**Table S5**). These unusual ratios, whether from experimental or optimized cell parameters, have been assumed to be due to more pronounced SOJT effects experienced by Nb^{5+} ions compared to Ta^{5+} ions.

3.4 Band structure and projected density of states (PDOS)

To confirm this hypothesis, band structures, density of states (DOSs), and orbital-resolved DOS were calculated. **Fig. 3** displays the calculated band structures of $NaNbO_2F_2$ and $NaTaO_2F_2$ along high symmetry lines. Both compounds are large gap insulators with an $E_{g,indirect/direct}$ of 3.40/3.48 and 3.86/3.88 eV for $NaNbO_2F_2$ and $NaTaO_2F_2$, respectively. The direct band gap occurs at the *Γ*-point for both compounds. It is worth mentioning that the band gaps computed at the DFT level are systematically underestimated with respect to experiments. Thus, state of the art calculations based on the GW approximation [77,78] might change the nature and ordering of the band gaps as self-energy corrections are not uniform across the Brillouin zone and depend on the compound.

As shown in the right panels of **Fig. 3**, the projected DOS (PDOS) of $NaNb(Ta)O_2F_2$ display a notable overlap between the electronic orbitals of the Nb(Ta) atoms and those of the O and F atoms across the whole energy region, demonstrating strong covalent interactions of the Nb(Ta)–O and Nb(Ta)–F bonds. The top of the valence band (VB) is mostly occupied by O and F 2*p* nonbonding states, while Nb(Ta) 4*d* (5*d*) orbitals are the main contributors to the bottom of the conduction band (CB). Interestingly, the bottom of the CB in $NaNbO_2F_2$ and $NaTaO_2F_2$ display different features while the top of the VB are quite similar. The main difference is related to the higher DOS at the VB maximum for $NaTaO_2F_2$ arising from a smaller bandwidth.

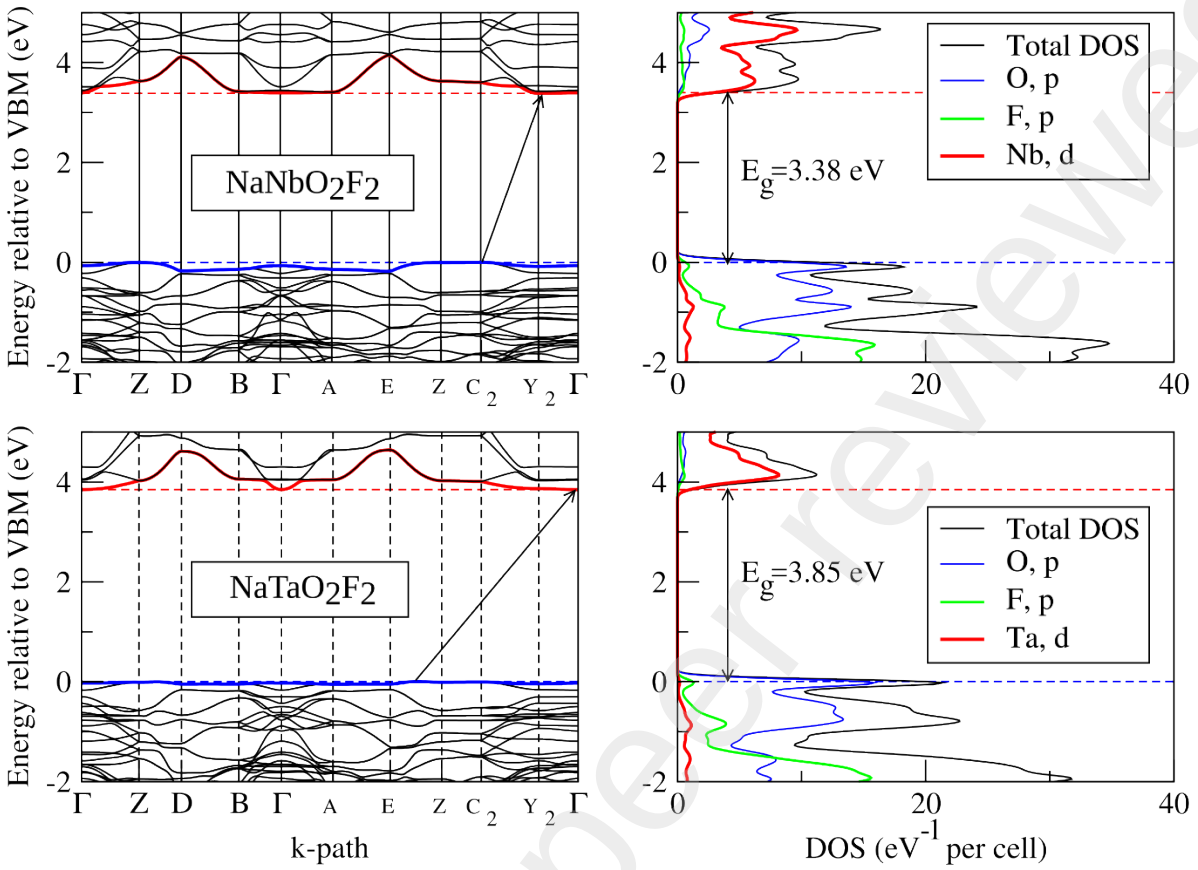

Fig. 3. Calculated DFT band structures from APO models along high symmetry lines and PDOS of $NaNbO_2F_2$ (upper panels) and $NaTaO_2F_2$ (lower panels). The position of the valence band maximum (VBM) and conduction band minimum (CBM) are respectively indicated as red and blue dashed lines. The arrows show the indirect band gaps from VBM to CBM.

To further understand the observed differences in the PDOS — the different features that the bottom of the CB display in $NaNbO_2F_2$ and $NaTaO_2F_2$ — and the role that SOJT effects plays in these differences, orbital-resolved DOS of both compounds was thoroughly investigated (**Fig. 4**). In heteroleptic polyhedral units (such as *cis*-$[MO_4F_2]^{5-}$ octahedra in this study), the magnitude of the distortion, characterized by short M–O and long M–F bonds, depends on the strength of the SOJT effect, which in turn is contingent on the strength of the hybridization between the empty *d* orbitals of cations and occupied *p* orbitals of anions [78–80]. The orbital-resolved DOS shows that for both O1 and O2 atoms, the 2*p* orbitals are primarily distributed from ~–4.8 eV to the Fermi energy (E_F) with a higher DOS distribution

near E_F. The 2p orbitals of F1 and F2 atoms are mainly distributed from ~–4.8 eV to E_F with a lower DOS distribution near E_F. This indicates that for both F and O atoms, the 2p orbitals are fully occupied. Meanwhile, the Nb(Ta) 4d(5d) orbitals are primarily distributed above E_F. However, finite DOS of $2p_x$ and $2p_y$ for O1 and $2p_z$ for O2 are located above E_F between ~4 and ~6 eV. In this energy range, major contributions from Nb(Ta) $4d_{xz}(5d_{xz})$, $4d_{yz}(5d_{yz})$, and $4d_{x^2-y^2}(5d_{x^2-y^2})$ are observed. This implies that there is hybridization between the unoccupied Nb(Ta) $4d_{xz}(5d_{xz})$, $4d_{yz}(5d_{yz})$, and $4d_{x^2-y^2}(5d_{x^2-y^2})$ orbitals and the occupied $2p_x$ and $2p_y$ for O1 and $2p_z$ for O2 orbitals, confirming the occurrence of SOJT effect in these compounds. The overlap between Nb(Ta) $4d_{xz}(5d_{xz})$ orbitals and the finite DOS observed above E_F for 2p orbitals of O1 and O2 being higher in $NaNbO_2F_2$ than in $NaTaO_2F_2$, the SOJT effect is stronger in $NaNbO_2F_2$, leading to longer Nb–O1 bonds than Ta–O1 bonds, and to the unusual difference observed for the c parameters of the studied compounds.

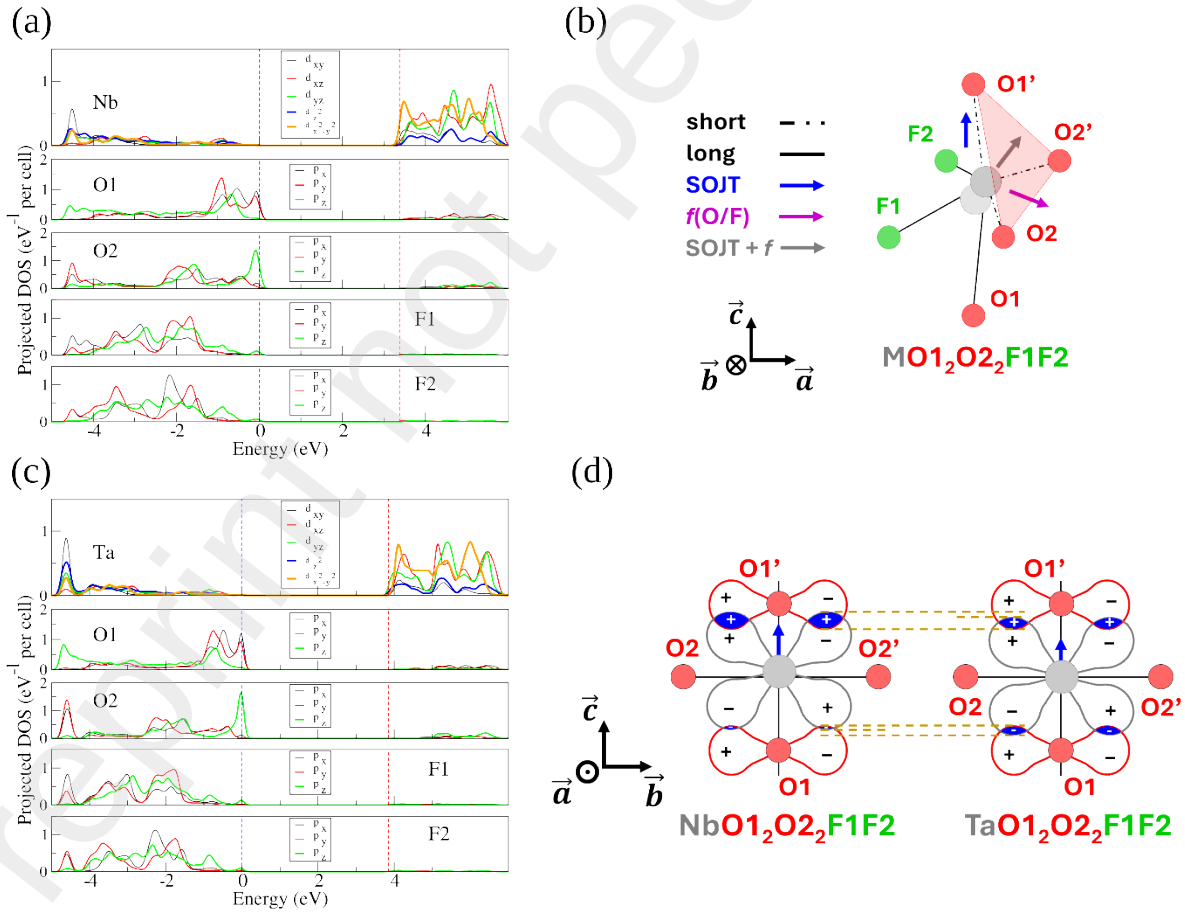

Fig. 4. Orbital-resolved Nb 4*d*, Ta 5*d*, O 2*p* and F 2*p* DOS for (a) $NaNbO_2F_2$ and (b) $NaTaO_2F_2$. (c) Off-centered $[NbO_4F_2]^{5-}$ octahedron and (d) illustration of the added covalent bonding due to distortions induced by the SOJTE. The overlap of the Nb (Ta) 4d (5d) orbital with the symmetry-adapted 2p orbital of the surrounding oxygen atoms is shown in blue. In In $[TaO_4F_2]^{5-}$ octahedron, the positive contribution in the overlap cancels the negative one so the net overlap is zero. In $[NbO_4F_2]^{5-}$ octahedron, the Nb atom is off-center, shifted in the z-direction, the net overlap gains a non-zero value.

Nevertheless, the structure of $NaNbO_2F_2$ determined by PXRD at RT does not show differences in Nb-O1 bond lengths (0.09 Å) as large as in the SC (0.29 Å) and APO (0.31 Å) structures (**Table 4**). In addition, except for Na, atoms in the structure of $NaNbO_2F_2$ determined by PXRD at RT, show higher, over double, IDPs values compared to those from $NaTaO_2F_2$ (**Table 2**). These observations could be explained by a dynamic and then in average weaker SOJT effect at RT in our sample, compared with the SOJT effects in the SC sample of Andersson and Galy [40] or predicted by DFT calculations (at 0 K).

3.5 PAW/GIPAW calculations

The calculated NMR parameters from the ES and APO models are given in **Table 8** and represented through comprehensive radar charts in **Fig. 5**, showcasing the relative difference, denoted as $f\{G;\mathrm{N}\}$, expressed as a percentage and defined by the relation $f\{G;N\} = 100 - \frac{|G_{exp} - G_{cal}|}{G_{exp}} \times 100$. G represents NMR parameters including δ_{iso}, C_{Q}, and η_{Q} and N refer to ^{19}F, ^{23}Na and ^{93}Nb nuclei. For ^{19}F in inorganic fluorides, several linear relationships between calculated σ_{iso} values, using the GIPAW approach, and experimental δ_{iso} values, $\delta_{\mathrm{iso}} = \sigma_{\mathrm{ref}} - a\,\sigma_{\mathrm{iso}}$, have been established to convert calculated σ_{iso} values into "calculated" δ_{iso} values. As the relationships are dependent on the metal atom(s) constituting the fluoride(s) [26,62,63], we considered the differences between the calculated σ_{iso} values and the experimental δ_{iso} values: $f\{\Delta;^{19}F\} = 100 - \frac{|\Delta\sigma_{iso} - \Delta\delta_{iso}|}{\Delta\sigma_{iso}} \times 100$.

These radar charts highlight the almost perfect agreement between the calculated and experimental NMR parameters calculated from APO structures, evidencing the efficiency of the DFT relaxation. The only exception is the η_{Q} value of ^{23}Na in $NaTaO_2F_2$, this parameter

being difficult to reproduce accurately. The agreement between experimental and calculated ^{93}Nb C_Q values is also improved. The ^{93}Nb C_Q value decreases due to the reduction of the radial distortions defined as $d_{X–Nb–X}$ - $\langle d \rangle$ (Å) with $d_{X–Nb–X}$ the sum of two opposite Nb–X (X = O, F) bond lengths and $\langle d \rangle$ the mean $d_{X–Nb–X}$ distance (**Table 7**) [82]. The C_Q value is not as small as expected for such small radial distortions likely due to the heteroanionic nature of the Nb octahedron.

For ^{19}F, the calculations confirm our tentative assignments since the calculated σ_{iso} of F1 is larger than those of F2 for both the compounds. The difference in σ_{iso} from APO structures is closer to the difference in δ_{iso} for both compounds. Furthermore, in agreement with slightly more intense spinning sidebands, the calculated σ_{CSA} values are higher for F2 atoms compared to F1 atoms (**Tables 5** and **8**). Two new linear relations have been established from NaF [55] and APO model of $NaNbO_2F_2$ ($\delta_{iso} = -0.706(15)\sigma_{iso} + 49.6(4.0)$), on the one hand (**Fig. S5**), and APO model of $NaTaO_2F_2$ ($\delta_{iso} = -0.741(1)\sigma_{iso} + 63.5(2)$), on the other hand (**Fig. S6**). These relations which could be useful in the future for the prediction of ^{19}F δ_{iso} values in Na and (Nb/Ta)-based (oxy)fluorides, have been used to calculate the ^{19}F δ_{iso} values of $NaNbO_2F_2$ and $NaTaO_2F_2$, respectively (**Table 8**).

Table 8. δ_{iso} (ppm), σ_{CSA} (ppm), η_{CSA}, C_Q (MHz) and η_Q values calculated for ^{19}F, ^{23}Na and ^{93}Nb atoms from the ES and APO models of $NaNbO_2F_2$ and $NaTaO_2F_2$.

Model	Nucleus	Site	σ_{iso}	δ_{iso}	σ_{CSA}	η_{CSA}	C_Q	η_Q
$NaNbO_2F_2$								
ES	^{19}F	F1	188.6	-83.5	74.2	0.67		
		F2	148.4	-55.1	-109.7	0.86		
	^{23}Na	Na1	567.4	-11.2	11.5	0.22	1.82	0.12
	^{93}Nb	Nb1	586.5	-1172.5	258.9	0.42	65.0	0.65
APO	^{19}F	F1	196.1	-88.8	-84.1	0.87		
		F2	161.9	-64.7	-113.2	0.75		
	^{23}Na	Na1	567.5	-11.2	10.0	0.34	1.66	0.69
	^{93}Nb	Nb1	576.8	-1163.7	258.8	0.27	43.2	0.58
$NaTaO_2F_2$								
ES	^{19}F	F1	225.2	-103.3	67.6	0.97		
		F2	177.0	-67.7	-103.7	0.85		
	^{23}Na	Na1	564.9	-9.1	10.8	0.30	1.78	0.92
APO	^{19}F	F1	224.6	-102.9	70.8	0.67		
		F2	195.3	-81.2	-90.0	0.88		
	^{23}Na	Na1	568.6	-12.2	9.9	0.39	1.78	0.95

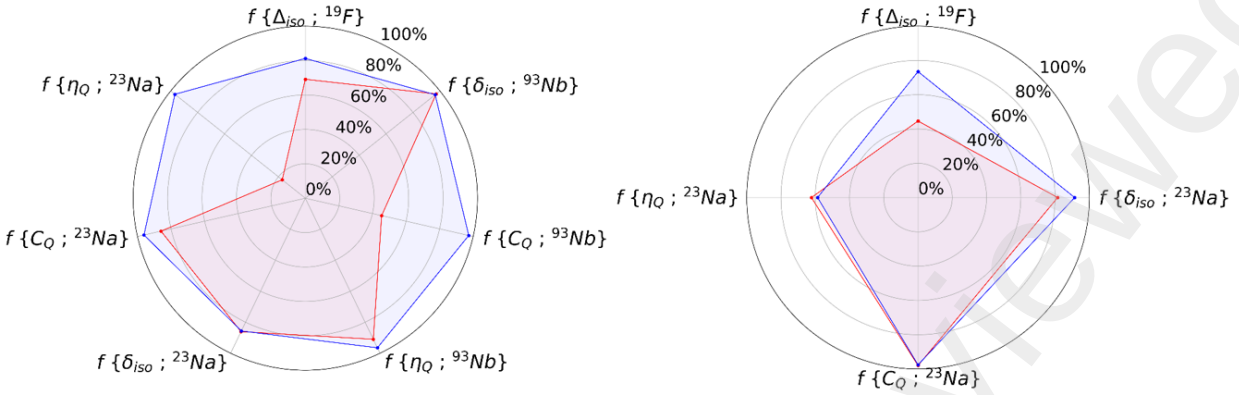

Fig. 5. Radar charts comparing experimental and calculated, from the ES (in red) and APO (in blue) models, NMR parameters of $NaNbO_2F_2$ (left) and $NaTaO_2F_2$ (right).

3.6 Thermal and temperature-controlled PXRD analysis

DTA-TGA were used to determine the thermal stability of the two studied compounds and the optimal annealing temperature to obtain samples as pure as possible. In the course of this study, we found that $NaNbO_2F_2$ exhibits a very low amplitude endothermic event around 240°C on heating up and one exothermic event with similar amplitude around 260°C on cooling down (hysteresis of ~20°C) whereas no similar event was detected for the tantalum isotype (**Fig. 6**). The TGA curves show no significant weight loss during these thermal treatments. Given the low intensity of these events, we have verified their reproducibility by running a second cycle (**Fig. S7**) immediately after the first (**Fig. 6**). Furthermore, additional experiments were performed on the $NaTaO_2F_2$ sample, up to 600°C, to ensure that the events observed in $NaNbO_2F_2$ do not occur at higher temperature in $NaTaO_2F_2$ (**Fig. S7**). A comparative structural study was then undertaken by temperature-controlled PXRD to elucidate this singular difference of thermal behavior.

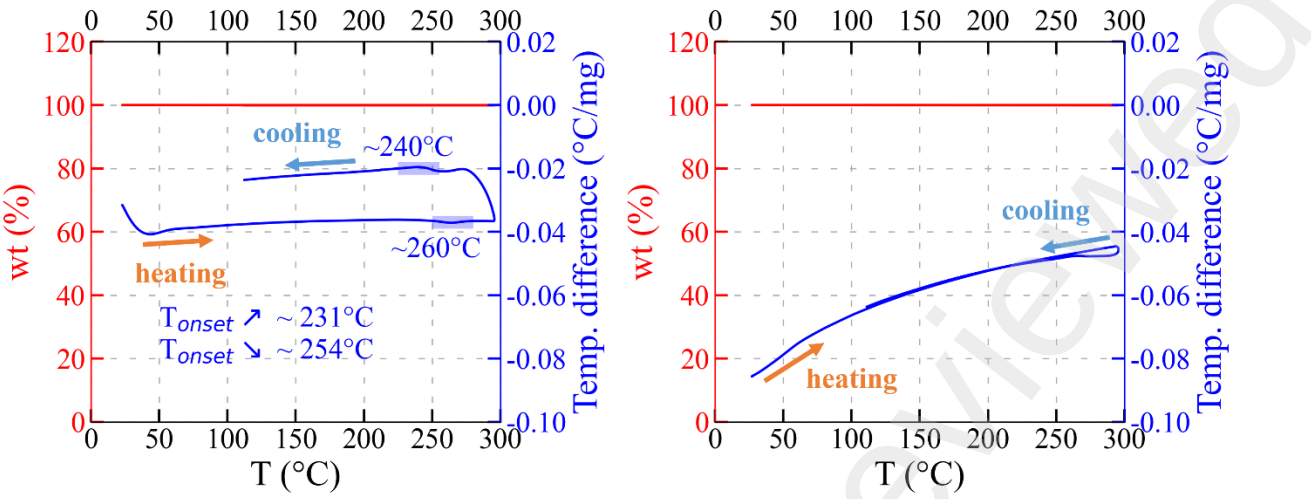

Fig. 6. DTA (blue) and TGA (red) curves of $NaNbO_2F_2$ (left) and $NaTaO_2F_2$ (right) recorded, under argon atmosphere (flow rate of 100 mL.min^{-1}), from RT to 300°C, with heating/cooling rate of 10°C.min^{-1}. The thermal accidents observed for $NaNbO_2F_2$ are highlighted in blue and their temperature values are indicated.

PXRD patterns were collected from 25 to 300°C for both compounds. For each compound, **Fig. 7** shows the temperature dependence of the PXRD diagrams from RT to 300°C in the 2θ range [32.5–35.5°] where most of the significant changes in peak intensity and position are observed**.** All the diffraction peaks move towards the low 2θ angles with increasing temperature, thus reflecting an expansion of the monoclinic cell in all three crystallographic directions. However, the displacement in position of the (300) peak with the temperature is greater for $NaNbO_2F_2$ than for $NaTaO_2F_2$, suggesting that the *a*-axis of the former has a greater expansion than that of the latter, which was confirmed by calculating the thermal expansion coefficients (TEC) along this axis (**Fig. 8**). For $NaNbO_2F_2$, this trend increases above 250°C particularly for the $(\bar{2}12)$ and (120) reflections (**Fig. 7**). The (020) and (112) reflections overlap at RT for $NaNbO_2F_2$ (**Fig. 7 (a)**), but are separated for $NaTaO_2F_2$ (**Fig. 7 (b)**). Conversely, the $(\bar{2}12)$ and (300) reflections are separated for $NaNbO_2F_2$ (**Fig. 7 (a)**) but overlap for $NaTaO_2F_2$ (**Fig. 7 (b)**). These differences in reflection positions are related to the differences in cell parameters (**Table 1**). While the *a* and *b* cell parameters of $NaTaO_2F_2$ are longer than those of $NaNbO_2F_2$, the *c* parameter of $NaTaO_2F_2$ is shorter. The initially

overlapped peaks start, gradually, separating upon reaching 300°C, especially the (020) and (112) peaks for $NaNbO_2F_2$ and the ($\bar{2}12$) and (300) for $NaTaO_2F_2$.

Rietveld refinements of the temperature-controlled PXRD data (**Figures S8-S15**) were achieved and the corresponding parameters and reliability factors are gathered in **Tables S9** and **S10**. The thermal evolutions of the cell parameters, *a*, *b*, *c* and *β* and volume *V* for both $NaNbO_2F_2$ (**Fig. 8** left) and $NaTaO_2F_2$ (**Fig. 8** right) were plotted and the corresponding thermal expansion coefficients (TEC, noted α) were determined. The thermal evolutions of the four cell parameters of $NaNbO_2F_2$ show the same trend: they increase linearly up to ~220°C and expand more strongly above this temperature (*i.e.* deviation). While the cell parameters *a*, *b* and *c* of $NaTaO_2F_2$ expand linearly in the whole temperature range explored, the expansion of the angle *β* shows a deviation above ~220°C but of a smaller magnitude than that observed for $NaNbO_2F_2$ (**Fig. 8**). In the [25-220°C] range, the unit cell of $NaTaO_2F_2$ homotetically expands in the (a,b) plane with increasing the temperature (identical α_a and α_b) but deforms strongly in the (a,c) plane (α_β is 7 and 10 times greater than α_a and α_c, respectively). Although the α_β coefficients are very close for the two compounds, the unit cell of $NaNbO_2F_2$ deforms along all three axes (significantly different values of α) with increasing the temperature.

For the two compounds, the thermal analyses and the thermal evolutions of the cell parameters are in agreement. Indeed, the departure from linearity in the thermal expansion of the cell parameters for $NaNbO_2F_2$ at ~220°C (**Fig. 8**) is unquestionably correlated with the endothermic peak detected in the DTA curve at ~231°C (**Fig. 6**) whereas nothing is observed for $NaTaO_2F_2$ in this temperature range. To identify the underlying factors contributing to this difference in the thermal behavior of these isostructural compounds, a thorough examination of various structural features was carried out.

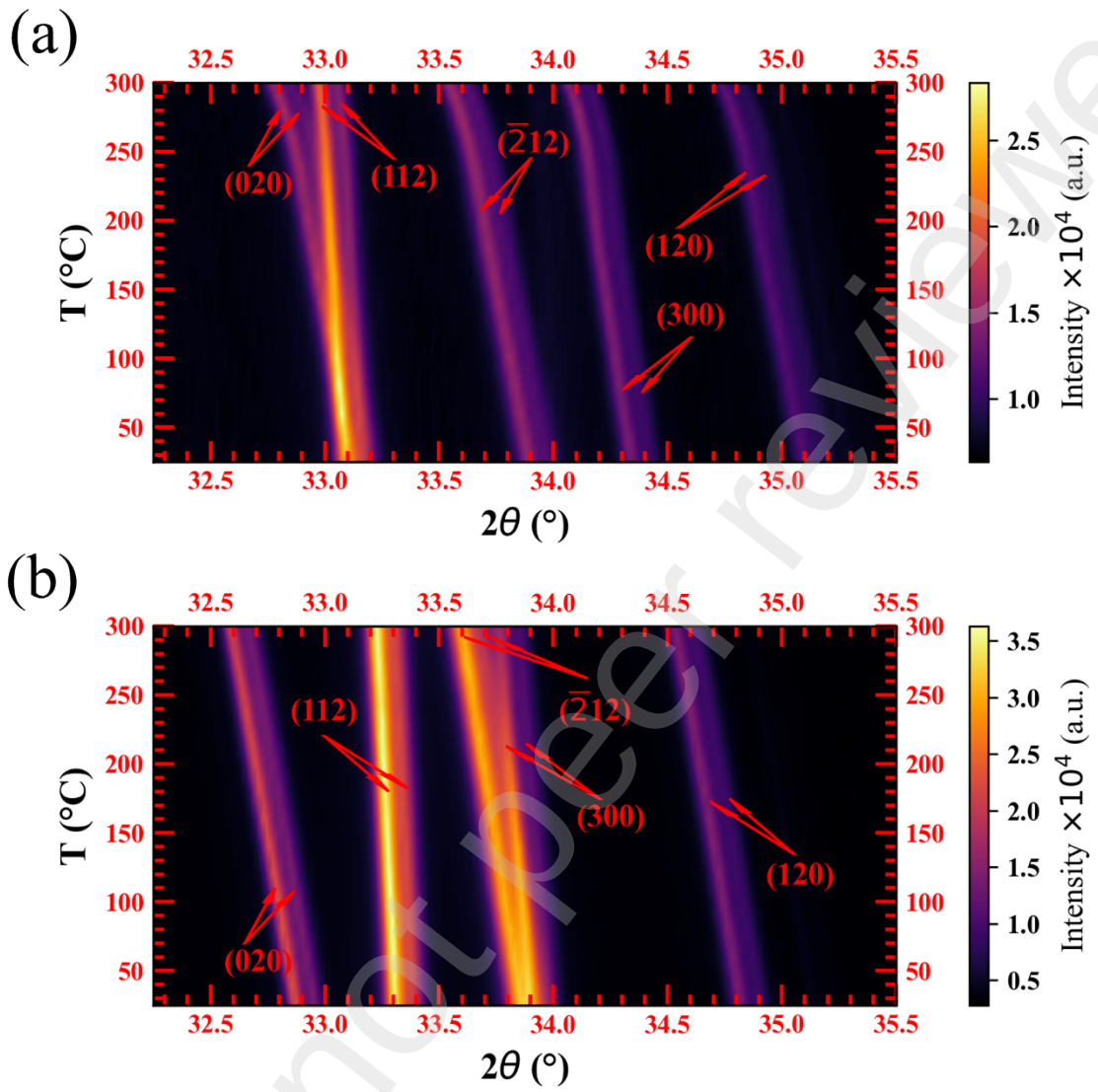

Fig. 7. Maps showing the temperature evolution of the (020), (112), ($\bar{2}$12), (300) and (120) peaks upon heating from RT to 300°C of $NaNbO_2F_2$ (a) and $NaTaO_2F_2$ (b).

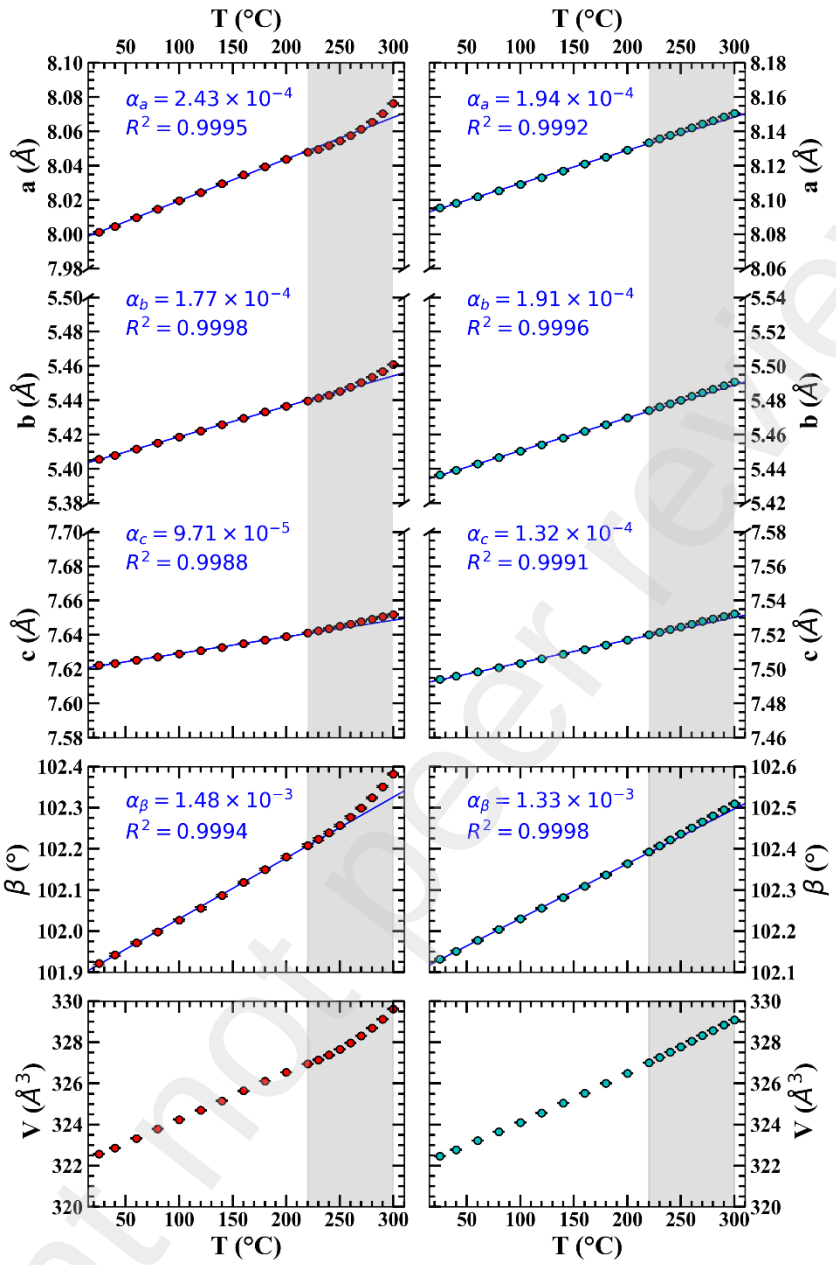

Fig. 8. Temperature dependence of the cell parameters *a*, *b*, *c*, *β* and *V* for $NaNbO_2F_2$ (left) and $NaTaO_2F_2$ (right) determined from Rietveld refinement of temperature-controlled PXRD data (**Tables S9** and **S10**). TECs (α_a, α_b, α_c and α_β, $°C^{-1}$), which were calculated from linear regressions in the [25–220°C] temperature range (blue line), are given as well as the R^2 values.

Fig. 9 (c) summarizes the evolution against temperature of M–F1 and M–O1 bond lengths and F1–M–O1 and O2–M–O1 angles from $[MO1_2O2_2F1F2]^{5-}$ octahedra (**Fig. 9 (a)**), the rest of the bond lengths and angles as well as those from $NaO1O2F1_3F2_3$ polyhedra are given as **SM** (**Fig. S16-S21)**. The evolutions of the inter-octahedral angles within the $(MO_2F_2)_n^{n-}$ layers are shown in **Fig. 10** and **11** for the (b,c) and (a,b) planes respectively, along with the layer thickness and distance between layers.

Despite variations in bond lengths and angles upon heating, the volumes of the octahedra in each compound vary only slightly (**Fig. 9 (b)**). $[TaO_4F_2]^{5-}$ octahedron presents more pronounced radial distortion, with a distribution of the lengths of its diagonals X–X of ~0.3 Å, in comparison to $[NbO_4F_2]^{5-}$ octahedron (~0.04 Å). For both octahedra, M–F(1,2) and M–O2' bond lengths vary slightly or remain stable over the [25-220°C] range (**Fig. 9 (c)** and **S18**). For the $[NbO_4F_2]^{5-}$ octahedron, the angle variations remain smaller than 2° (**Fig. S19-S21**), while two bond lengths show significant variations (0.09 Å for Nb–O1 and -0.11 Å for Nb–O1', **Fig. 9 (c)**). As both the diagonal O1–O1' length and O1-Nb-O1' angle within the $[NbO_4F_2]^{5-}$ octahedron remain constant, there is a marked decentering of the Nb atom, resulting in one short (1.85 Å) and three relatively close (1.98, 2.00 and 2.11 Å) Nb–O bond lengths at 220°C (**Fig. 9 (c)**). In contrast, the angle variations in the $[TaO_4F_2]^{5-}$ octahedron are more important (up to 4.9° for F1–Ta–O2 and 3.9° for F2–Ta–O2', **Fig. S19**), yet the bond length variations remain less significant than in $[NbO_4F_2]^{5-}$ octahedron (**Fig. 9 (c) and S18**). Three bond lengths exhibit variations exceeding 2%, resulting in a notably short Ta–O2 (1.79 Å), one relatively short Ta–O1 (1.91 Å) and two longer Ta–O1' and Ta–O2' (2.09 and 2.10 Å) bond lengths, and indicating a displacement of the Ta atom from the octahedron center toward O2 and O1 atoms at 220°C (**Fig. 9 (c)**). Despite their different thermal evolutions of the distances and angles, the high gap between the distortion indices (DI) of the octahedron in $NaNbO_2F_2$ and $NaTaO_2F_2$ (**Fig. 9 (d)**) does not change in the range [25-220°C]. For $NaNbO_2F_2$, in the [220-300°C] range, the difference between the opposite Nb–O1 and Nb–O1' bond lengths decreases (**Fig. 9 (c)**), in contrast to what was observed previously, while the diagonal O1–O1' length remains more or less constant. Given the small angular variations (**Fig. S19-S21**), this indicates a shift of the Nb position back towards the center of the octahedron, indicating a decrease of the SOJT effect above 220°C. In addition, both Nb–F1 bond length and diagonal F1–O2' length decrease by ~0.04 Å, while the Nb–O2' bond length

remains stable (**Fig. 9 (c)**), leading to an increase in radial distortion for the $[NbO_4F_2]^{5-}$ octahedron.

In the [25-220°C] temperature range, the volumes (V_p) of the NaO_2F_6 polyhedra increase (~0.8 to 0.9 $Å^3$, **Fig. S17**). Between 220 and 300°C, the V_p value remains stable for $NaNbO_2F_2$ but continues to increase for $NaTaO_2F_2$. This can be related to the evolution of the Na–O1 and Na–O2 bond lengths, which both increased markedly up to 220° (between 0.06 and 0.20 Å) and then remains stable for $NaNbO_2F_2$ whereas Na–O2 bond length continues to increase for $NaTaO_2F_2$ (~0.06 Å, **Fig. S17**).

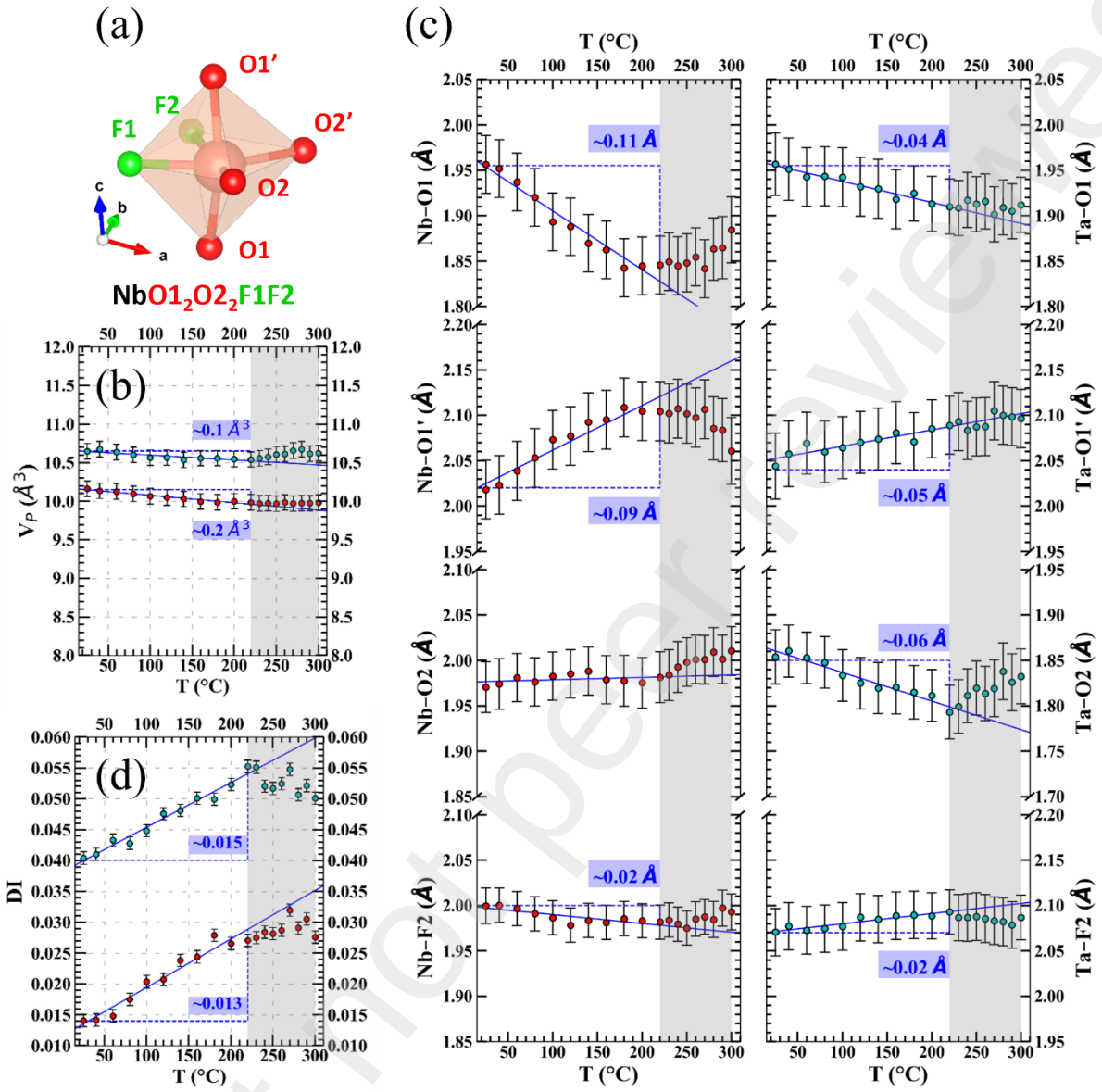

Fig. 9. (a) Perspective view of $[NbO1_2O2_2F1F2]^{5-}$ octahedron, in which, atoms labeled X and X' (X = O1 and O2) are equivalent by symmetry operations. Temperature dependence of (b) $[MO_4F_2]^{5-}$ octahedron volume, (c) bond lengths and (d) distortion index of $NaNbO_2F_2$ (red dots) and $NaTaO_2F_2$ (blue dots). Linear regressions (blue lines) are plotted in the [25–220°C] temperature range guiding the evolution of each quantity. The amplitude of significant evolutions is highlighted in blue.

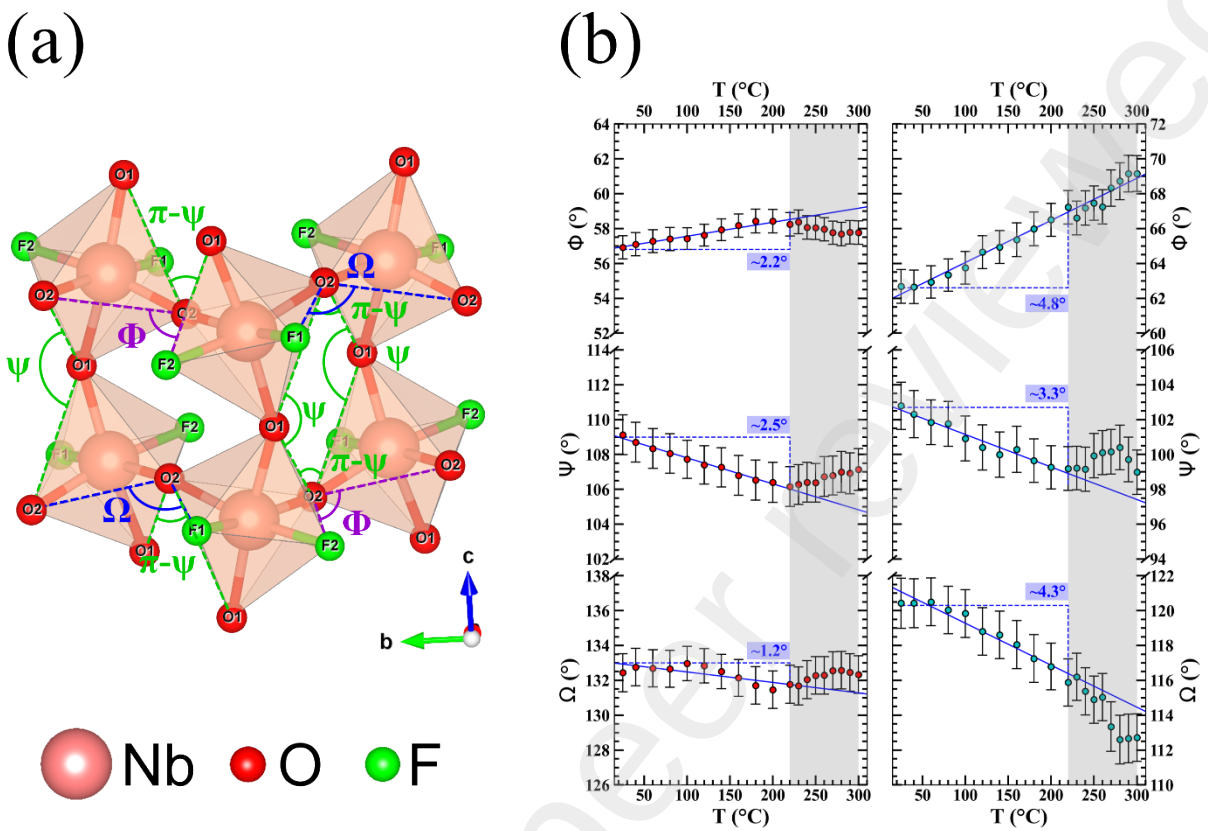

Fig. 10. Perspective view of the smallest octahedron unit describing the $NaNbO_2F_2$ framework with the inter-octahedral angles (Φ, Ψ, and Ω) (a). Inter-octahedral angles from $NaNbO_2F_2$ (left (b)) and $NaTaO_2F_2$ (right (b)) as a function of temperature. Linear regressions (blue lines) are plotted in the [25–220°C] temperature range guiding the evolution of each quantity. The amplitude of significant evolutions is highlighted in blue.

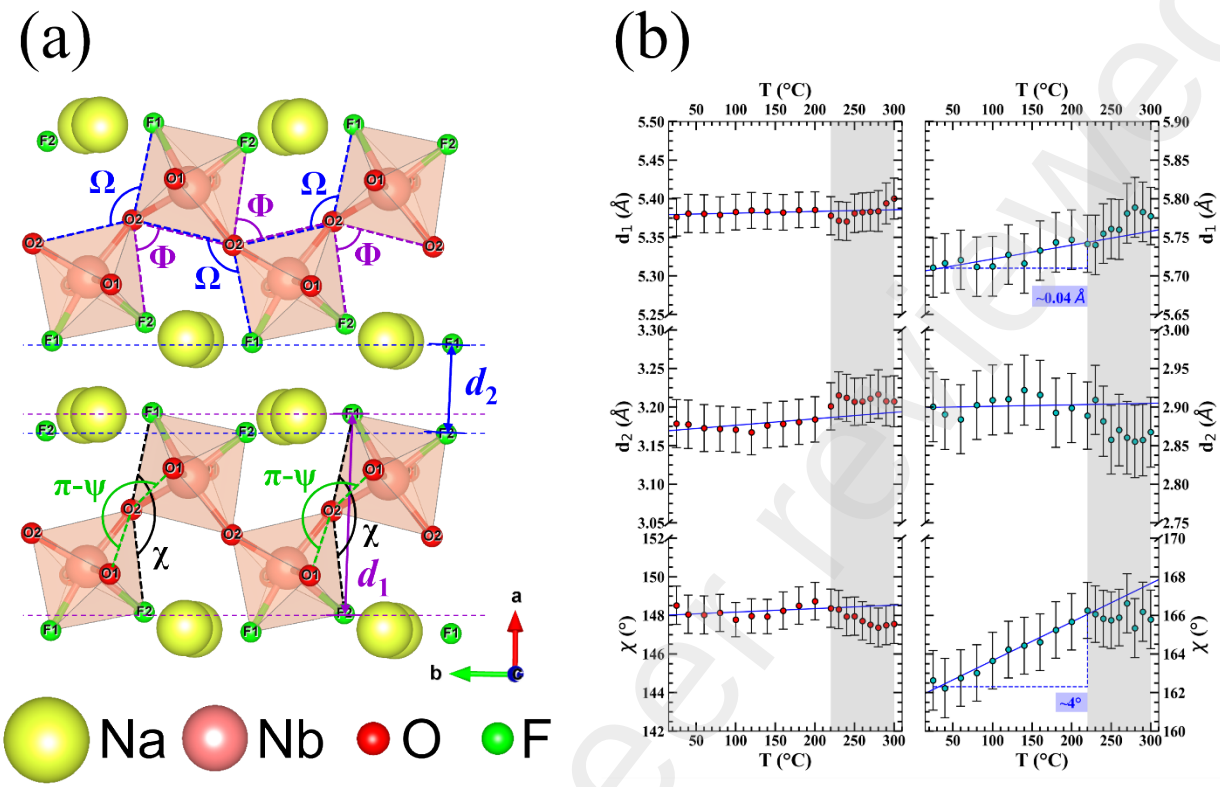

Fig. 11. (a) Illustration of two $(NbO_2F_2)_n^{n-}$ layers with indicated inter-octahedral angles (χ, Ψ and Ω), layer thickness (d_1) and distance between layers (d_2). (b) χ, d_1 and d_2 from $NaNbO_2F_2$ (left (b)) and $NaTaO_2F_2$ (right (b)) as a function of temperature. Linear regressions (blue lines) are plotted in the [25–220°C] temperature range guiding the evolution of each quantity. The amplitude of significant evolutions is highlighted in blue.

The differences between the compounds are not only present at the polyhedral level but also in the $(MO_2F_2)_n^-$ layers. In the (b,c) plane (**Fig. 10**), all the octahedra are connected by neighboring O atoms, with four octahedra forming a parallelogram (O1,O2,O1,O2). Its evolution against temperature can be followed using the inter-octahedron O2–O1–O2 angle, Ψ, and its complementary angle, π-Ψ (**Fig. 10**). In the [25–220°C] range, Ψ value decreases by ~3° and the (O1,O2,O1,O2) parallelogram approaches a rectangle, more for $NaTaO_2F_2$ than for $NaNbO_2F_2$., thus explaining the difference in α_c between the two compounds. In the (a,b) plane (**Fig. 11**), the opposite O2–O2–F1 and O2–O2–F2 angles, noted Ω and Φ respectively, and the F1–O2–F2 angle, χ, provide information about the unfolding of the $(MO_2F_2)_n^-$ layers along the b axis (Ω and Φ) and the a-axis (χ). In the [25–220°C] range and

for both compounds, Φ and χ increase whereas Ω decreases, but with a higher magnitude for $NaTaO_2F_2$. The zigzag form of the $(TaO_2F_2)_n^-$ layers is stretched, mostly along the *b* axis with the marked increase (decrease) in Φ (Ω) values by more than 6° at 300°C. This stretching is further reinforced by the evolution against temperature of χ (**Fig. 11**), which is increasing by ~4° and may partially explain the slight increase of the $(TaO_2F_2)_n^-$ layer thickness, d_1. In $NaNbO_2F_2$, the layers are initially more corrugated (57°, 133°, 109° and 148° for Φ, Ω, Ψ and χ, respectively); the stretching is limited (opening of Φ angle by 2.2°) and the layer thickness, d_1, remains constant (**Fig. 11**). No further stretching is observed for this compound at higher temperatures ([220–300°C]).

4. Conclusion

$NaNbO_2F_2$ and $NaTaO_2F_2$ compounds were prepared using solid-state synthesis, and characterized using PXRD, ^{19}F NMR, and high-field ^{23}Na and ^{93}Nb NMR. For each compound, the atomic positions were optimized and the NMR parameters were calculated for ES and APO models. These parameters were subsequently compared to the experimental data, revealing that the APO models are more precise than the ES ones. Furthermore, these structural models revealed that $NaNbO_2F_2$ experienced second-order Jahn-Teller distortion, further confirmed by band structure and projected density of states calculations. This explains the unusual observed disparity between the cell parameters, particularly *c*, which is related to the Nb–O1 bond length. The observed low amplitude endothermic event was confirmed by the evolution against temperature of the cell parameters derived from Rietveld refinement of the VT PXRD data. For $NaNbO_2F_2$, these parameters evolve linearly with temperature until reaching ~220°C, close to the endothermic event temperature, after which the parameter evolution deviated from linearity. In contrast, for $NaTaO_2F_2$, and except for β, cell parameters exhibited linear evolution with no deviation observed above ~220°C. A thorough analysis of structural parameters at different temperatures revealed distinct behaviors of the two compounds. Notably, $NaTaO_2F_2$ exhibit significant evolutions of the angles between polyhedra with the stretching of the zigzag form in the $(TaO_2F_2)_n^-$ layers, mostly along the *b* axis, while $NaNbO_2F_2$ display strong evolutions of the bond lengths, especially opposite Nb–O1 and Nb–O1' which indicates a variation of the SOJT strength with the temperature.

CRediT authorship contribution statement

Ouail Zakary: Conceptualization, Formal analysis, Investigation, Validation, Data Curation, Writing - Original Draft, Writing - Review & Editing, Visualization. **Monique Body:** Conceptualization, Writing - Review & Editing, Supervision, Project administration, Funding acquisition. **Vincent Sarou-Kanian:** Investigation. **Brice Arnaud:** Investigation, Visualization, Writing - Review & Editing. **Gwenaël Corbel:** Conceptualization, Investigation, Writing - Review & Editing. **Christophe Legein:** Conceptualization, Writing - Review & Editing, Supervision, Project administration, Funding acquisition.

Declaration of competing interest

The authors declare that they have no known competing financial interests or personal relationships that could have appeared to influence the work reported in this paper.

Data availability

All datasets, and plotting scripts created in this paper are publicly available in the GitHub repository: https://github.com/clegein/data-NaMO2F2. The repository includes, (*i*) experimental and Rietveld refinement data for RT and temperature-controlled PXRD diagrams, (*ii*) DTA and TGA data, (*iii*) both experimental and fitted data of solid-state NMR spectra of ^{19}F, ^{23}Na, and ^{93}Nb nuclei, (*iv*) input and output VASP files for DFT calculations (including geometry optimization and NMR parameter calculations), (*v*) Python scripts and raw numerical data for all figures used in the manuscript and supplementary materials.

Supplementary material

The supplementary material is available free of charge at: link TBA.

An overview on cell parameters of isotypes niobium (V) and tantalum (V) oxyfluorides, fluorides and oxides; Rietveld refinements; $NaNbO_2F_2$ and $NaTaO_2F_2$ structural features; ^{19}F and ^{23}Na MAS NMR spectra and their fits; new linear relations $\delta_{iso} = \sigma_{ref} - a\ \sigma_{iso}$ from NaF and APO models of $NaNbO_2F_2$ and $NaTaO_2F_2$; thermal and temperature controlled PXRD analysis.

Accession codes

CCDC 2298195 and 2298196 contain the supplementary crystallographic data of the RT structures for $NaNbO_2F_2$ and $NaTaO_2F_2$, respectively. These data can be obtained free of charge via https://www.ccdc.cam.ac.uk/structures, or by emailing data_request@ccdc.cam.ac.uk, or by contacting The Cambridge Crystallographic Data Center, 12 Union Road, Cambridge CB2 1EZ, UK; fax: +44 1223336033.

Acknowledgments

Financial support from the IR INFRANALYTICS FR2054 for conducting the research is gratefully acknowledged. The authors would like to thank Franck Fayon (CEMHTI) for

reading the manuscript, his support with the NMR experiments and his advice on the reconstruction of ^{23}Na NMR spectra.

References

[1] H. Kageyama, K. Hayashi, K. Maeda, J.P. Attfield, Z. Hiroi, J.M. Rondinelli, K.R. Poeppelmeier, Expanding frontiers in materials chemistry and physics with multiple anions, Nat Commun 9 (2018) 772. https://doi.org/10.1038/s41467-018-02838-4.

[2] J.K. Harada, N. Charles, K.R. Poeppelmeier, J.M. Rondinelli, Heteroanionic Materials by Design: Progress Toward Targeted Properties, Adv. Mater. 31 (2019) 1805295. https://doi.org/10.1002/adma.201805295.

[3] H.K. Izumi, J.E. Kirsch, C.L. Stern, K.R. Poeppelmeier, Examining the Out-of-Center Distortion in the $[NbOF_5]^{2-}$ Anion, Inorg. Chem. 44 (2005) 884–895. https://doi.org/10.1021/ic048766d.

[4] H. Lu, R. Gautier, M.D. Donakowski, T.T. Tran, B.W. Edwards, J.C. Nino, P.S. Halasyamani, Z. Liu, K.R. Poeppelmeier, Nonlinear Active Materials: An Illustration of Controllable Phase Matchability, J. Am. Chem. Soc. 135 (2013) 11942–11950. https://doi.org/10.1021/ja4050604.

[5] Y. Hu, C. Wu, X. Jiang, Z. Wang, Z. Huang, Z. Lin, X. Long, M.G. Humphrey, C. Zhang, Giant Second-Harmonic Generation Response and Large Band Gap in the Partially Fluorinated Mid-Infrared Oxide $RbTeMo_2O_8F$, J. Am. Chem. Soc. 143 (2021) 12455–12459. https://doi.org/10.1021/jacs.1c06061.

[6] M. Yan, R.-L. Tang, W. Liu, S.-P. Guo, From $Ba_3Nb_2O_2F_{12}(H_2O)_2$ to $Ba_{0.5}NbO_2F_2(H_2O)$: Achieving Balanced Nonlinear Optical Performance by O/F Ratio Regulation, Inorg. Chem. 61 (2022) 20709–20715. https://doi.org/10.1021/acs.inorgchem.2c03842.

[7] V.V. Atuchin, T.A. Gavrilova, V.G. Kesler, M.S. Molokeev, K.S. Aleksandrov, Low-temperature synthesis and structural properties of ferroelectric $K_3WO_3F_3$ elpasolite, Chemical Physics Letters 493 (2010) 83–86. https://doi.org/10.1016/j.cplett.2010.05.023.

[8] A.M. Fry, P.M. Woodward, Structures of α-$K_3MoO_3F_3$ and α-$Rb_3MoO_3F_3$: Ferroelectricity from Anion Ordering and Noncooperative Octahedral Tilting, Crystal Growth & Design 13 (2013) 5404–5410. https://doi.org/10.1021/cg401342q.

[9] L. Xu, H. Gong, L. Deng, F. Long, Y. Gu, J. Guan, Complex-Mediated Synthesis of Tantalum Oxyfluoride Hierarchical Nanostructures for Highly Efficient Photocatalytic Hydrogen Evolution, ACS Appl. Mater. Interfaces 8 (2016) 9395–9404. https://doi.org/10.1021/acsami.6b02622.

[10] K. Aihara, R. Mizuochi, M. Okazaki, S. Nishioka, S. Yasuda, T. Yokoi, F. Ishiwari, A. Saeki, M. Inada, K. Maeda, Low-Temperature Microwave-Assisted Hydrothermal Synthesis of $Pb_2Ti_2O_{5.4}F_{1.2}$ Photocatalyst for Improved H_2 Evolution under Visible Light, ACS Materials Lett. 5 (2023) 2355–2360. https://doi.org/10.1021/acsmaterialslett.3c00574.

[11] J.C. Pérez-Flores, R. Villamor, D. Ávila-Brande, J.M. Gallardo Amores, E. Morán, A. Kuhn, F. García-Alvarado, VO_2F: a new transition metal oxyfluoride with high specific capacity for Li ion batteries, J. Mater. Chem. A 3 (2015) 20508–20515. https://doi.org/10.1039/C5TA05434F.

[12] J.T. Incorvati, L.F. Wan, B. Key, D. Zhou, C. Liao, L. Fuoco, M. Holland, H. Wang, D. Prendergast, K.R. Poeppelmeier, J.T. Vaughey, Reversible Magnesium Intercalation into a Layered Oxyfluoride Cathode, Chem. Mater. 28 (2016) 17–20. https://doi.org/10.1021/acs.chemmater.5b02746.

[13] D. Deng, Transition Metal Oxyfluorides for Next-Generation Rechargeable Batteries, ChemNanoMat 3 (2017) 146–159. https://doi.org/10.1002/cnma.201600342.

[14] R.D. Shannon, Revised effective ionic radii and systematic studies of interatomic distances in halides and chalcogenides, Acta Cryst A 32 (1976) 751–767. https://doi.org/10.1107/S0567739476001551.

[15] J. Dabachi, M. Body, C. Galven, F. Boucher, C. Legein, Preparation-Dependent Composition and O/F Ordering in NbO_2F and TaO_2F, Inorg. Chem. 56 (2017) 5219–5232. https://doi.org/10.1021/acs.inorgchem.7b00355.

[16] M.E. Welk, A.J. Norquist, F.P. Arnold, C.L. Stern, K.R. Poeppelmeier, Out-of-Center Distortions in d^0 Transition Metal Oxide Fluoride Anions, Inorg. Chem. 41 (2002) 5119–5125. https://doi.org/10.1021/ic025622v.

[17] M.R. Marvel, J. Lesage, J. Baek, P.S. Halasyamani, C.L. Stern, K.R. Poeppelmeier, Cation–Anion Interactions and Polar Structures in the Solid State, J. Am. Chem. Soc. 129 (2007) 13963–13969. https://doi.org/10.1021/ja074659h.
[18] R.A.F. Pinlac, C.L. Stern, K.R. Poeppelmeier, New Layered Oxide-Fluoride Perovskites: $KNaNbOF_5$ and $KNaMO_2F_4$ ($M = Mo^{6+}, W^{6+}$), Crystals 1 (2011) 3–14. https://doi.org/10.3390/cryst1010003.
[19] M. Holland, N. Charles, J.M. Rondinelli, K.R. Poeppelmeier, Reconstructive Transitions from Rotations of Rigid Heteroanionic Polyhedra, J. Am. Chem. Soc. 138 (2016) 11882–11889. https://doi.org/10.1021/jacs.6b06813.
[20] H. Jo, M.H. Lee, K.M. Ok, Order and Disorder: Toward the Thermodynamically Stable α-$BaMoO_2F_4$ from the Metastable Polymorph, Chem. Mater. 33 (2021) 1875–1882. https://doi.org/10.1021/acs.chemmater.1c00074.
[21] F.J. Brink, L. Norén, D.J. Goossens, R.L. Withers, Y. Liu, C.-N. Xu, A combined diffraction (XRD, electron and neutron) and electrical study of $Na_3MoO_3F_3$, Journal of Solid State Chemistry 174 (2003) 450–458. https://doi.org/10.1016/S0022-4596(03)00303-7.
[22] A.M. Fry, H.A. Seibel, I.N. Lokuhewa, P.M. Woodward, $Na_{1.5}Ag_{1.5}MO_3F_3$ (M = Mo, W): An Ordered Oxyfluoride Derivative of the $LiNbO_3$ Structure, J. Am. Chem. Soc. 134 (2012) 2621–2625. https://doi.org/10.1021/ja208587e.
[23] H.-X. Tang, R.-B. Fu, Z.-J. Ma, X.-T. Wu, A Potassium Tungsten Oxyfluoride with Strong Second-Harmonic Generation Response Derived from Anion-Ordered Functional Motif, Inorg. Chem. 60 (2021) 17364–17370. https://doi.org/10.1021/acs.inorgchem.1c02861.
[24] S. Bai, D. Wang, H. Liu, Y. Wang, Recent advances of oxyfluorides for nonlinear optical applications, Inorg. Chem. Front. 8 (2021) 1637–1654. https://doi.org/10.1039/D0QI01156H.
[25] R.L. Withers, F.J. Brink, Y. Liu, L. Norén, Cluster chemistry in the solid state: Structured diffuse scattering, oxide/fluoride ordering and polar behaviour in transition metal oxyfluorides, Polyhedron 26 (2007) 290–299. https://doi.org/10.1016/j.poly.2006.05.021.
[26] O. Zakary, M. Body, T. Charpentier, V. Sarou-Kanian, C. Legein, Structural Modeling of O/F Correlated Disorder in $TaOF_3$ and $NbOF_{3-x}(OH)_x$ by Coupling Solid-State NMR and DFT Calculations, Inorg. Chem. 62 (2023) 16627–16640. https://doi.org/10.1021/acs.inorgchem.3c02844.
[27] E.E. McCabe, I.P. Jones, D. Zhang, N.C. Hyatt, C. Greaves, Crystal structure and electrical characterisation of Bi_2NbO_5F: an Aurivillius oxide fluoride, J. Mater. Chem. 17 (2007) 1193. https://doi.org/10.1039/b613970a.
[28] A. Agulyansky, Chemistry of Tantalum and Niobium Fluoride Compounds, Elsevier, 2004. https://doi.org/10.1016/B978-0-444-51604-6.X5000-9.
[29] S. Andersson, R. Ottinger, S.J. Cyvin, I. Fedorcsák, R.A. Hoffman, A. Westerdahl, The Crystal Structure of $NaNb_6O_{15}F$ and $NaNb_6O_{15}OH$, Acta Chem. Scand. 19 (1965) 2285–2290. https://doi.org/10.3891/acta.chem.scand.19-2285.
[30] R. Stomberg, K.-M. Marstokk, H. Møllendal, H. Priebe, D.L. Powell, R. Suchi, The Crystal Structure of alpha-Sodium Hexafluorooxoniobate(V), alpha-$Na_3[NbF_6O]$., Acta Chem. Scand. 37a (1983) 453–459. https://doi.org/10.3891/acta.chem.scand.37a-0453.
[31] R. Stomberg, S. Jagner, A.F. Andresen, M. Maeda, H. Ohtaki, The Crystal Structure of Sodium Pentafluorooxoniobate(2–), $Na_2[NbF_5O]$., Acta Chem. Scand. 38a (1984) 603–607. https://doi.org/10.3891/acta.chem.scand.38a-0603.
[32] J. Köhler, A. Simon, $NaNb_3O_5F$ – eine Niob-Niob-Dreifachbindung mit „side-on"-Koordination durch Nb-Atome, Angew. Chem. 98 (1986) 1011–1012. https://doi.org/10.1002/ange.19860981118.
[33] D.X. Li, The crystal structure of $Na_3Nb_{12}O_{31}F$, Journal of Solid State Chemistry 73 (1988) 1–4. https://doi.org/10.1016/0022-4596(88)90045-X.

[34] D.X. Li, S. Hovmöller, The crystal structure of $Na_3Nb_{12}O_{31}F$ determined by HREM and image processing, Journal of Solid State Chemistry 73 (1988) 5–10. https://doi.org/10.1016/0022-4596(88)90046-1.
[35] E. Boivin, F. Pourpoint, S. Saitzek, P. Simon, P. Roussel, H. Kabbour, An unusual O^{2-}/F^- distribution in the new pyrochlore oxyfluorides: $Na_2B_2O_5F_2$ (B = Nb, Ta), Chem. Commun. 58 (2022) 2391–2394. https://doi.org/10.1039/D1CC06760E.
[36] M. Vlasse, J.-P. Chaminade, J.-C. Massies, M. Pouchard, Structure de l'oxyfluorure de tantale et de sodium $Na_2Ta_2O_5F_2\beta$, Journal of Solid State Chemistry 12 (1975) 102–109. https://doi.org/10.1016/0022-4596(75)90184-X.
[37] J.B. Goodenough, H.Y.-P. Hong, J.A. Kafalas, Fast Na^+-ion transport in skeleton structures, Materials Research Bulletin 11 (1976) 203–220. https://doi.org/10.1016/0025-5408(76)90077-5.
[38] J.-P. Chaminade, M. Pouchard, P. Hagenmuller, Tantalates et oxyfluorotantalates de sodium, Revue de Chimie Minérale 9 (1972) 381–402.
[39] J.-P. Chaminade, M. Pouchard, Cristallochimie des composés oxygénés, oxyfluorés et fluorés du tantale et des alcalins ou de l'argent, Annales de Chimie 10 (1975) 75–99.
[40] S. Andersson, J. Galy, The crystal structure of $NaNbO_2F_2$, Acta Crystallogr B Struct Sci 25 (1969) 847–850. https://doi.org/10.1107/S056774086900313X.
[41] I.D. Brown, D. Altermatt, Bond-valence parameters obtained from a systematic analysis of the Inorganic Crystal Structure Database, Acta Crystallographica Section B Structural Science 41 (1985) 244–247. https://doi.org/10.1107/S0108768185002063.
[42] N.E. Brese, M. O'Keeffe, Bond-valence parameters for solids, Acta Crystallographica Section B Structural Science 47 (1991) 192–197. https://doi.org/10.1107/S0108768190011041.
[43] B.M. Fung, A.K. Khitrin, K. Ermolaev, An Improved Broadband Decoupling Sequence for Liquid Crystals and Solids, Journal of Magnetic Resonance 142 (2000) 97–101. https://doi.org/10.1006/jmre.1999.1896.
[44] D. Massiot, F. Fayon, M. Capron, I. King, S. Le Calvé, B. Alonso, J.-O. Durand, B. Bujoli, Z. Gan, G. Hoatson, Modelling one- and two-dimensional solid-state NMR spectra: Modelling 1D and 2D solid-state NMR spectra, Magn. Reson. Chem. 40 (2002) 70–76. https://doi.org/10.1002/mrc.984.
[45] P. Hohenberg, W. Kohn, Inhomogeneous Electron Gas, Phys. Rev. 136 (1964) B864–B871. https://doi.org/10.1103/PhysRev.136.B864.
[46] G. Kresse, J. Furthmüller, Efficient iterative schemes for *ab initio* total-energy calculations using a plane-wave basis set, Phys. Rev. B 54 (1996) 11169–11186. https://doi.org/10.1103/PhysRevB.54.11169.
[47] G. Kresse, J. Furthmüller, Efficient iterative schemes for *ab initio* total-energy calculations using a plane-wave basis set, Phys. Rev. B 54 (1996) 11169–11186. https://doi.org/10.1103/PhysRevB.54.11169.
[48] J.P. Perdew, K. Burke, M. Ernzerhof, Generalized Gradient Approximation Made Simple, Phys. Rev. Lett. 77 (1996) 3865–3868. https://doi.org/10.1103/PhysRevLett.77.3865.
[49] P.E. Blöchl, Projector augmented-wave method, Phys. Rev. B 50 (1994) 17953–17979. https://doi.org/10.1103/PhysRevB.50.17953.
[50] G. Kresse, D. Joubert, From ultrasoft pseudopotentials to the projector augmented-wave method, Phys. Rev. B 59 (1999) 1758–1775. https://doi.org/10.1103/PhysRevB.59.1758.
[51] C.J. Pickard, F. Mauri, All-electron magnetic response with pseudopotentials: NMR chemical shifts, Phys. Rev. B 63 (2001) 245101. https://doi.org/10.1103/PhysRevB.63.245101.
[52] J.R. Yates, C.J. Pickard, F. Mauri, Calculation of NMR chemical shifts for extended systems using ultrasoft pseudopotentials, Phys. Rev. B 76 (2007) 024401. https://doi.org/10.1103/PhysRevB.76.024401.
[53] U. Haeberlen, In Advances in Magnetic Resonance, Suppl. 1; J. S. Waugh, Ed.; Academic Press (1976).

[54] M. Biswal, M. Body, C. Legein, G. Corbel, A. Sadoc, F. Boucher, Structural Investigation of α- and β-Sodium Hexafluoroarsenate, $NaAsF_6$, by Variable Temperature X-ray Powder Diffraction and Multinuclear Solid-State NMR, and DFT Calculations, J. Phys. Chem. C 116 (2012) 11682–11693. https://doi.org/10.1021/jp3040727.
[55] V.T. Deshpande, Thermal expansion of sodium fluoride and sodium bromide, Acta Cryst 14 (1961) 794–794. https://doi.org/10.1107/S0365110X61002357.
[56] H.M. Rietveld, A profile refinement method for nuclear and magnetic structures, J Appl Crystallogr 2 (1969) 65–71. https://doi.org/10.1107/S0021889869006558.
[57] J. Rodriguez-Carvajal, MAGNETIC STRUCTURE DETERMINATION FROM POWDER DIFFRACTION USING THE PROGRAM *FullProf*, in: Applied Crystallography, WORLD SCIENTIFIC, Wisla, Poland, 2001: pp. 30–36. https://doi.org/10.1142/9789812811325_0005.
[58] C.R. Groom, I.J. Bruno, M.P. Lightfoot, S.C. Ward, The Cambridge Structural Database, Acta Crystallogr B Struct Sci Cryst Eng Mater 72 (2016) 171–179. https://doi.org/10.1107/S2052520616003954.
[59] R.M. Wood, G.J. Palenik, Bond Valence Sums in Coordination Chemistry. Sodium−Oxygen Complexes, Inorg. Chem. 38 (1999) 3926–3930. https://doi.org/10.1021/ic9903331.
[60] K. Momma, F. Izumi, *VESTA* : a three-dimensional visualization system for electronic and structural analysis, J Appl Crystallogr 41 (2008) 653–658. https://doi.org/10.1107/S0021889808012016.
[61] W.L. Roth, O. Muller, Study, selection, and preparation of solid cationic conductors. Final report, 13 November 1972--12 November 1973, General Electric Co., Schenectady, N.Y. (USA), 1974. https://www.osti.gov/biblio/5083602 (accessed August 21, 2023).
[62] A. Sadoc, M. Body, C. Legein, M. Biswal, F. Fayon, X. Rocquefelte, F. Boucher, NMR parameters in alkali, alkaline earth and rare earth fluorides from first principle calculations, Phys. Chem. Chem. Phys. 13 (2011) 18539. https://doi.org/10.1039/c1cp21253b.
[63] M. Biswal, M. Body, C. Legein, A. Sadoc, F. Boucher, NbF_5 and TaF_5: Assignment of ^{19}F NMR resonances and chemical bond analysis from GIPAW calculations, Journal of Solid State Chemistry 207 (2013) 208–217. https://doi.org/10.1016/j.jssc.2013.09.001.
[64] M. Boča, A. Rakhmatullin, J. Mlynáriková, E. Hadzimová, Z. Vasková, M. Mičušík, Differences in XPS and solid state NMR spectral data and thermo-chemical properties of iso-structural compounds in the series $KTaF_6$, K_2TaF_7 and K_3TaF_8 and $KNbF_6$, K_2 NbF_7 and K_3NbF_8, Dalton Trans. 44 (2015) 17106–17117. https://doi.org/10.1039/C5DT02560E.
[65] D. Massiot, F. Fayon, M. Deschamps, S. Cadars, P. Florian, V. Montouillout, N. Pellerin, J. Hiet, A. Rakhmatullin, C. Bessada, Detection and use of small J couplings in solid state NMR experiments, Comptes Rendus Chimie 13 (2010) 117–129. https://doi.org/10.1016/j.crci.2009.05.001.
[66] M. Murakami, Y. Noda, K. Takegoshi, Terminal and bridging fluorine ligands in TiF_4 as studied by ^{19}F NMR in solids, Solid State Nuclear Magnetic Resonance 101 (2019) 82–88. https://doi.org/10.1016/j.ssnmr.2019.05.007.
[67] H. Bode, H. Von Döhren, Die Kristallstruktur des Kaliumhexafluoroniobats und des Kaliumhexafluorotantalats, Acta Cryst 11 (1958) 80–82. https://doi.org/10.1107/S0365110X58000220.
[68] R.W. Berg, J.H. von Barner, E. Christensen, K. Nielsen, The Crystal Structure and IR and Raman Spectra of alpha-$CsNbF_6$, in: Progress in Molten Salt Chemistry 1, Prof. Niels J. Bjerrum Special Volume, Ed. R.W. Berg and H.A. Hjuler, Elsevier, n.d.: pp. 75–94. https://orbit.dtu.dk/en/publications/the-crystal-structure-and-ir-and-raman-spectra-of-alpha-csnbf6.
[69] S.D. Griesemer, L. Ward, C. Wolverton, High-throughput crystal structure solution using prototypes, Phys. Rev. Materials 5 (2021) 105003. https://doi.org/10.1103/PhysRevMaterials.5.105003.

[70] Z. Gan, P. Gor'kov, T.A. Cross, A. Samoson, D. Massiot, Seeking Higher Resolution and Sensitivity for NMR of Quadrupolar Nuclei at Ultrahigh Magnetic Fields, J. Am. Chem. Soc. 124 (2002) 5634–5635. https://doi.org/10.1021/ja025849p.
[71] O.B. Lapina, D.F. Khabibulin, A.A. Shubin, V.V. Terskikh, Practical aspects of ^{51}V and ^{93}Nb solid-state NMR spectroscopy and applications to oxide materials, Progress in Nuclear Magnetic Resonance Spectroscopy 53 (2008) 128–191. https://doi.org/10.1016/j.pnmrs.2007.12.001.
[72] L.-S. Du, R.W. Schurko, N. Kim, C.P. Grey, Solid-State ^{93}Nb, ^{19}F, and ^{113}Cd Nuclear Magnetic Resonance Study of Niobium Oxyfluorides: Characterization of Local Distortions and Oxygen/Fluorine Ordering, J. Phys. Chem. A 106 (2002) 7876–7886. https://doi.org/10.1021/jp020457q.
[73] C. Martineau, M. Body, C. Legein, G. Silly, J.-Y. Buzaré, F. Fayon, Multinuclear High-Resolution NMR Study of Compounds from the Ternary System NaF−CaF_2−AlF_3 : from Determination to Modeling of NMR Parameters, Inorganic Chemistry 45 (2006) 10215–10223. https://doi.org/10.1021/ic061348j.
[74] G. Silly, C. Legein, J.Y. Buzaré, F. Calvayrac, Electric field gradients in fluoride crystalline powders: correlation of NMR measurements with ab initio calculations, Solid State Nuclear Magnetic Resonance 25 (2004) 241–251. https://doi.org/10.1016/j.ssnmr.2003.09.001.
[75] W.H. Baur, The geometry of polyhedral distortions. Predictive relationships for the phosphate group, Acta Crystallogr B Struct Sci 30 (1974) 1195–1215. https://doi.org/10.1107/S0567740874004560.
[76] K. Robinson, G.V. Gibbs, P.H. Ribbe, Quadratic Elongation: A Quantitative Measure of Distortion in Coordination Polyhedra, Science 172 (1971) 567–570. https://doi.org/10.1126/science.172.3983.567.
[77] B. Arnaud, M. Alouani, All-electron projector-augmented-wave GW approximation: Application to the electronic properties of semiconductors, Phys. Rev. B 62 (2000) 4464–4476. https://doi.org/10.1103/PhysRevB.62.4464.
[78] S. Lebègue, B. Arnaud, M. Alouani, P.E. Bloechl, Implementation of an all-electron GW approximation based on the projector augmented wave method without plasmon pole approximation: Application to Si, SiC, AlAs, InAs, NaH, and KH, Phys. Rev. B 67 (2003) 155208. https://doi.org/10.1103/PhysRevB.67.155208.
[79] R.A. Wheeler, M.Hwan. Whangbo, Timothy. Hughbanks, Roald. Hoffmann, J.K. Burdett, T.A. Albright, Symmetric vs. asymmetric linear M-X-M linkages in molecules, polymers, and extended networks, J. Am. Chem. Soc. 108 (1986) 2222–2236. https://doi.org/10.1021/ja00269a018.
[80] M. Kunz, I.D. Brown, Out-of-Center Distortions around Octahedrally Coordinated d0 Transition Metals, Journal of Solid State Chemistry 115 (1995) 395–406. https://doi.org/10.1006/jssc.1995.1150.
[81] H. Sun, K. Deng, E. Kan, Y. Du, Second-order Jahn–Teller effect induced high-temperature ferroelectricity in two-dimensional NbO_2X (X = I, Br), Nanoscale Adv. 5 (2023) 2979–2985. https://doi.org/10.1039/D3NA00245D.
[82] M. Body, C. Legein, J.-Y. Buzaré, G. Silly, P. Blaha, C. Martineau, F. Calvayrac, Advances in Structural Analysis of Fluoroaluminates Using DFT Calculations of ^{27}Al Electric Field Gradients, The Journal of Physical Chemistry A 111 (2007) 11873–11884. https://doi.org/10.1021/jp0740696.